MASTER'S THESIS:

Unveiling PNe in early-type galaxies

FACULTY OF SCIENCES

Master in Astrophysics

Pablo M. Galán de Anta

Supervisor:

Jesús Falcón Barroso (Instituto de Astrofísica de Canarias)

Marc Sarzi (University of Hertfordshire)

2 de julio de 2018

Resumen

Las nebulosas planetarias (PNe) son empleadas como medidores de distancia a través de la llamada Función de Luminosidad (LF por sus siglas en inglés), una ley estándar definida por la magnitud absoluta de las nebulosas presentes en galaxias de tipo temprano. Para obtener esta ley se recurre a medir la magnitud absoluta de las nebulosas a través del doblete de [OIII], una transición prohibida que solo se produce bajo ciertas condiciones físicas presentes en estos objetos. La LF no depende de la metalicidad, es por esto que es una candela estándar empleada como calibrador secundario de distancias. No obstante, la metalicidad de las nebulosas sí aporta información sobre el tipo de población progenitora del que proceden. Por otra parte, la cinemática de estos objetos permite comparar con las estrellas subyacentes y así desvelar el origen interno o externo de las nebulosas.

En este trabajo se estudian las nebulosas planetarias en galaxias de tipo temprano y espirales con el objetivo de desentrañar el origen de estos objetos. Para ello analizamos la cinemática de las nebulosas y su relación con las estrellas subyacentes, es por ello que el estudio se remite a galaxias de canto para poder obtener la velocidad radial de estos objetos. Así mismo, estudiamos la distribución de magnitudes absolutas a través de la LF. Por último, analizamos la relación metalicidad-luminosidad de las nebulosas para buscar la conexión de estas con sus estrellas progenitoras. El estudio se remite a cuatro galaxias del cúmulo de Fornax: FCC 153, FCC 167, FCC 170 y FCC 177. Los datos son proporcionados por la unidad de campo integral MUSE en el Very Large Telescope como parte del proyecto Fornax3D.

Para detectar las nebulosas presentes en las galaxias hemos sustraído el continuo de nuestras observaciones para analizar las regiones de emisión, en concreto las regiones que emiten en el doblete de [OIII]. Detectamos las distintas fuentes puntuales aplicando el programa *SExtractor* que nos proporciona las coordenadas de estas fuentes. Para discriminar entre fuentes que son PNe y falsas detecciones comparamos la forma de nuestro espectro con el ajuste que resulta de aplicar gaussianas al doblete de [OIII]. Caracterizamos la Point Spread Function (PSF) a través de las nebulosas más brillantes de cada una de las galaxias. Empleando la PSF del instrumento podemos obtener los espectros de las nebulosas planetarias y por tanto, caracterizar sus propiedades.

A partir de los espectros hemos obtenido la cinemática de las nebulosas estimando la posición del centroide de la línea de 5007 Å desplazada al rojo. A través de la cinemática podemos discernir entre aquellas nebulosas que han sido originadas en la propia galaxia y aquellas que proceden del propio cúmulo o incluso fuentes a redshift elevado cuyo espectro es similar al de las nebulosas. Por otro lado, los espectros nos permiten obtener la magnitud absoluta de cada nebulosa a través del flujo obtenido del doblete de [OIII]. Bineando las magnitudes absolutas de las nebulosas obtenemos la distribución de magnitudes en función del número de nebulosas.

Estudiando la cinemática hemos observado una buena concordancia entre las nebulosas y las estrellas subyacentes. Este hecho confirma que las nebulosas son capaces de describir en un buen grado de aproximación el movimiento de las estrellas. La cinemática nos ha permitido identificar la presencia de "outliers" entre nuestras detecciones, objetos que caen fuera del fondo de estrellas y que por tanto, no podemos incluir en el análisis. Por otra parte, las velocidades obtenidas nos permiten confirmar que todas las nebulosas se han originado dentro de las propias galaxias dado que ninguna posee una velocidad mayor a 350 km/s respecto al centro galáctico.

Respecto a la función de luminosidad, hemos comprobado que su distribución se ajusta a la ley estándar descrita en Ciardullo et al. (1989). Observamos como la magnitud absoluta de la nebulosa más brillante de cada galaxia no supera el valor estándar de $M^\star_{5007} = -4{,}47$ dado por diversos autores como Ciardullo et al. (2005); Merrett et al. (2006); Sarzi et al. (2011). Comprobamos que las nebulosas más tenues de las cuatro galaxias sufren el llamado "sesgo de incompletitud", y que para dichas nebulosas nuestras distribuciones se desvían de la ley estándar debido a que no podemos observar las más tenues.

Como análisis final hemos tratado de relacionar la metalicidad del medio en el que están embebidas las PNe con el número de nebulosas detectadas. Para ello hemos obtenido la metalicidad de las estrellas subyacentes a través de modelos de poblaciones estelares. Relacionando el número de PNe con la metalicidad del medio hemos observado que no existe una correspondencia clara entre ambas cantidades. Este hecho puede ser debido a la baja significancia en el número de PNe detectadas a causa del método de detección empleado.

El único hecho deducido de este análisis es que las nebulosas más brillantes se encuentran en zonas ricas en metales.

Este trabajo es un anticipo de un estudio mucho más amplio a realizar con todas las galaxias (de tipo temprano y espirales) del cúmulo de Fornax para los que hay datos de Fornax3D. La muestra completa nos permitirá mejorar la estadística presentada en este trabajo y aportar más información sobre el origen de las PNe y su relación con su entorno.

Palabras clave: Nebulosas planetarias; galaxia de tipo temprano; espectros; doblete de [OIII]; cinemática; función de luminosidad; metalicidad.

Contents

List of Figures

List of Tables

Chapter 1

Introduction

The Planetary Nebulae (PNe) are easy to detect due to their characteristic emission in the [OIII] doublet, which allows to observe them in external galaxies in a few Mpc (Ciardullo et al., 2004; Coccato et al., 2009; Marigo et al., 2004; Pastorello et al., 2013; Sarzi et al., 2011). Otherwise, these objects emit high amount of light in the [OIII] doublet and are located in regions where the stellar light background extinction is negligible (Ciardullo et al., 1989). The so-called Luminosity Function (LF) of the PNe is obtained through the absolute magnitude of these objects and serves as distance indicator through its universal cut-off which is yet poorly understood. This cut-off is given by the absolute magnitude of the brightest nebula which is defined as $M_{5007}^\star = -4.47 \pm 0.05$ for Early-Type Galaxies (ETGs) with well-determined Cepheid distances, due to the initial magnitude with which the PNe begin in their evolutionary tracks (Merrett et al., 2006). This distance indicator competes in accuracy with calibrators as Cepheids and the Surface Brightness Fluctuations (SBF) (Ciardullo et al., 2002). Moreover, the LF can be modelled by a standard law (Ciardullo et al., 1989), which involves the brightest cut-off of the PNe distribution. On the other hand, the PNe are along with the globular clusters, a tracer of the kinematics for radii greater than $2R_e$, where the light of the stars is too faint to be measured (Coccato et al., 2009). For all of these reasons, the PNe represent a good tool of analysis for extragalactic physics.

The presence of the nebula around the remnant core of the progenitor star produces the scatter of light, and consequently the characteristic spectrum emitted by a Planetary Nebula (PN). This kind of clouds possess a high amount of ionised atomic species such as [HII], [HeII], [HeIII], [OIII] and [OVI]. Particularly, the non-metallic ionic species ([HII] and [HeIII]) do not produce emission lines and the abundance of [OIII] is higher than the presence of [OVI] for the external regions of the cloud and it is greater than the abundance of [HeII] along the whole cloud (Marigo et al., 2004). For these reasons, the [OIII] doublet dominates the spectrum of the PNe and represents the main feature to detect these objects. This doublet corresponds to a forbidden transition of two lines: 4959 Å and 5007 Å . In the past, this rare transition was supposed to be the so-called "nebulium". It is produced in a concrete conditions of extreme low density in where the electrons occupy excited metastable energy levels which could not be occupied in other conditions (Kwok, 2007).

Measuring the spectra of the PNe it is possible to determine the intensity of the [OIII] doublet and consequently the LF (Ciardullo et al., 2005). One of the most interesting features of the LF is the fact that the absolute magnitude of the brightest PN does not depend on the galaxy type (Ciardullo et al., 2005; Jacoby, 1989; Rodríguez-González et al., 2015). On the other hand, the abundance dependence of the oxygen inside the PN is cancelled by the opacity of the own nebula around the progenitor star (Ciardullo et al., 2005). This fact implies that the LF does not depend on metallicity. On the other hand, those models that reproduce the LF not just have to adjust to its shape, but also to the invariance of three different criteria which involves the own LF standard law (Ciardullo et al., 2002): the invariance of the brightest absolute magnitude; the mean value of it; and the number of bright planetary nebulae which populate the end of the LF. The last constrain can be used to estimate the percentage of stars that contributes to the end of the LF. The density of the PNe per bolometric luminosity at the end of LF gives a clue of the percentage of stars per bright PN. This parameter is determined through evolutionary stellar tracks which provide the stellar evolutionary flux, the time that a PN spends in the bright-[OIII] state, and the fraction of stars which turning off the main sequence to become a bright PNe (Buzzoni et al., 2006).

The LF is equally valid to calibrate distances for elliptical and spiral galaxies (Ciardullo et al., 2005) and represents not just an important standard candle to measure extragalactic distances, but also to give an estimation of number of progenitor stars (Rodríguez-González et al., 2015). In Buzzoni et al. (2006) they

study the ratio between the number of PNe and the luminosity of the galaxy, relating them with the age and metallicity of the progenitor stars through Single Stellar Population (SSP) models. They estimate that the number of PNe formed in a typical galaxy of $10^{11} M_\odot$ is between $1 - 6$ PNe per $10^7 L_\odot$ stars, and this ratio is constant for all Hubble types. This ratio is related with the lifetime of the PNe, and the shorter the ratio, the shorter the lifetime of the PNe.

The evolution of the luminosity of the PN for a typical PNe evolutionary model (Marigo et al., 2004) is given by a timescale of $\tau_{PN} \sim 10^3 - 10^4$ years (Buzzoni et al., 2006; Rodríguez-González et al., 2015). This timescale defines the time interval for which the luminosity of the PNe falls off from its brightest stage to fainter stages. Due to the expansion of the nebula the gas density diminishes, consequently, the brightness of the nebula decreases too and the absolute magnitude suffers a displacement to larger values (less negative). However, the formation of new PNe due to lower mass stars, will replace the decrease in the brightness of the PNe which have become fainter. Models like developed by Schönberner et al. (2007) show how the luminosity of PNe decreases with time due to the expansion of the gas and the reduction in density of ionising photons. This scenario implies that brightest nebulae eventually will move away from to bright end of the LF.

Many studies where the LF is studied show a huge lack of PNe as from a peak in absolute magnitude from which the number of PNe rapidly falls. This is dued by the so-called "incompleteness" (Merrett et al., 2006; Sarzi et al., 2011), an observational bias produced by the detection limit of the used instrument which cannot allow us to detect the total amount of the PNe, overall the faintest ones. Because of this fact, the standard law which modelizes the LF (Ciardullo et al., 1989) needs to take into account this bias. Moreover, this lack implies that our total number of detected PNe is far from the ideal scenario for which we would have on the order of $20 - 40$ times more detected PNe (Buzzoni et al., 2006).

The mass of the progenitor stars determines the mass of the remnant star, and consequently the absolute magnitude of the PNe (Sarzi et al., 2011). Indeed, the brightest nebula is due to a first generation of intermediate mass stars in the host galaxies which leaves a remnant star in the core of the nebula with around $0.7 M_\odot$ (Marigo et al., 2004). This fact means that for the same absolute magnitude, there are a stellar population with similar age and mass, so the LF relates not just the distance as a function of $M_{5007}^\star$, but also the age of a progenitor population with its absolute magnitude.

For high mass PN cores of over $1 M_\odot$, Ciardullo et al. (2005) arguments that the binary coalescence due to the blue-stragglers[1] is able to increase the initial core mass from $0.7 M_\odot$ to $1 M_\odot$. This process is relatively abundant in ETGs. On the other hand, for PNe in the mid range of core masses between $0.5 M_\odot$ and $0.6 M_\odot$ the absolute magnitude falls in ranges of the mean values for a typical LF (Ciardullo et al., 2005; Sarzi et al., 2011), which corresponds to the common situation for Sun like progenitor stars which represent more than the 90% of the stars in the universe. Indeed, the higher the absolute magnitude, the lesser the mass of the PNe and consequently, the mass of the progenitor stars. For ETGs in which the abundance of Population II stars are greater than in late types (and consequently, the presence of blue-stragglers too) it would be expected that the presence of the brightest PNe would be produced by blue-stragglers or intermediate mass stars.

In Ciardullo et al. (2005) they study the relevance of binary stars in the formation of PNe cores for $M_{core} > 0.6 M_\odot$ for different type of galaxies: E0, Sb, Sbc and Sc. The analysis shows how the fraction of PNe derived from binary systems diminishes with time to reach a plateau of 0.2 of the total fraction of PNe for star formation rate with solar-metallicity assumed. On the other hand, this fraction reach a constant value of around 0.4 of the total for core masses of coalesced binaries which have been enhanced by 10% of their initial mass. So in both cases, the contribution of binary-evolved objects contribute to all type of stellar populations.

Another magnitude which serves as dynamic indicator of the galaxies is the kinematics of PNe. The kinematics represents a good tool to determine the movement of the underlying stars, and to detect the presence of outliers, objects which may have an extragalactic origin (Coccato et al., 2009; Pulsoni et al., 2017; Spiniello et al., 2018). For instance, the domain of velocity is typically for disk-like galaxies, while the domain of the velocity dispersion is for elliptical galaxies (Cappellari and Emsellem, 2004). Because of this, comparing the PNe kinematics with the movement of the stars, is possible to glimpse the relation between the PNe and their progenitor stars as well as to observe the presence of different substructures into the host

---

[1]Blue-stragglers are stars present in ancient structures as globular clusters which look younger than they really are. This kind of stars are explained through two hypothesis: (i) merge of two red giants or (ii) binary system in which the main component receive material from the second one (Mapelli et al., 2006). In both cases, the system results in a blue massive star brighter than it should be after many billions of years of stellar evolution. This type of object are relatively common in globular clusters where the density of the objects is high and the collision between them is also high. Globular clusters as NGC 6362 show the presence of this blue-stragglers.

galaxy. On the other hand, the peculiar velocities of the PNe may give us clues about their origin within the cluster. Those PNe with high velocities may have been formed in the outskirts of the host galaxy and proceed from a galaxy that interacts with it (Coccato et al., 2009; Spiniello et al., 2018).

Many studies of PNe for their kinematics or their LF are performed over disk-like galaxies as M31 (Ciardullo et al., 1989; Merrett et al., 2006; Pastorello et al., 2013) and due to the closeness of this galaxy with respect to Milky Way, the studies may be skew to the central part of M31, providing information about their progenitor stars and the presence of substructures within the bulge. For spiral galaxies like Andromeda, the metallicity of the stellar populations has been proved to be intrinsically related with the number of PNe through their initial absolute magnitude (Sarzi et al., 2011). In other studies as Buzzoni et al. (2006) focused on ETGs, it has been observed that more metal-rich stellar populations may also have a lower specific number of PNe. At a given mass, metal-rich stars loose more mass during their RGB phase preventing them to produce PNe. Consequently, we see fewer of them in the most massive and metal-rich galaxies. However this remains to be properly tested, in particular since PNe and stellar-metallicity measurements were taken from different regions of the Buzzoni et al. (2006) galaxies, namely halo PNe versus central stellar metallicity measurements.

The data which we have analysed are provided by the F3D project[2]. In this work, we study the contribution of PNe to the kinematics of four ETGs located in Fornax cluster[3]: FCC 153, FCC 167, FCC 170 and FCC 177. With the kinematics of this kind of objects obtained, we can compare with the stellar background kinematics in order to observe discrepancies between them which may provide information about the internal or external origin of the nebulae. On the other hand, we estimate the luminosity function for this galaxies in order to prove if its shape may be fitting by the observational law provided by Ciardullo et al. (1989). Moreover, we extend the study to analyse the metallicity of the galaxies to relate it with the number of PNe. In this way, we can relate the different populations of detected PNe with the different populations of stars in order to deduce the origin and evolution of the PNe (Sarzi et al., 2011).
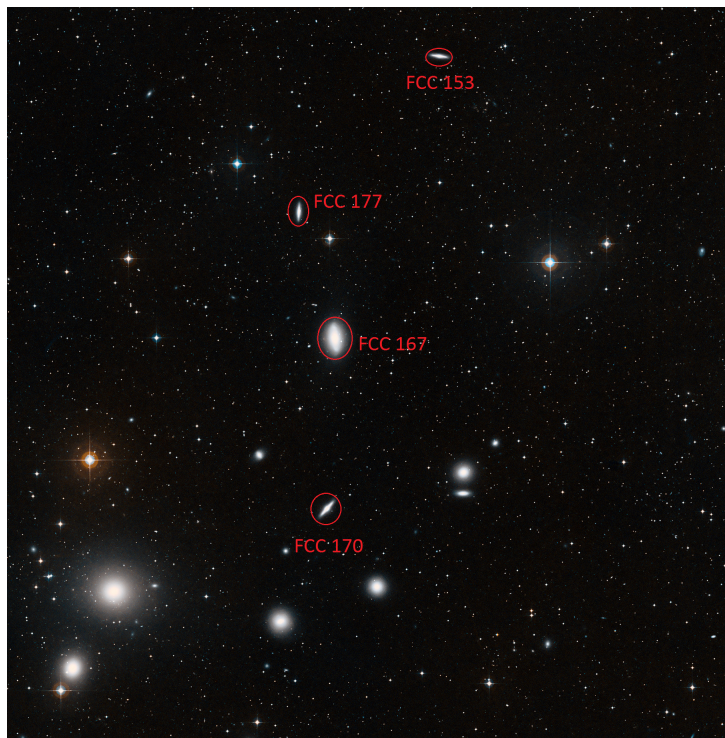
Figure 1.1: Fornax cluster and the four galaxies of study: FCC 153, FCC 167, FCC 170 and FCC 177. Image credit: ESO and Digitized Sky Survey 2.

---

[2]The Fornax3D project consists in a survey of the Fornax cluster in order to analyse the properties of the ETGs and the role played by mergers. The project may be consult on `http://www.na.astro.it/Fornax3D/Fornax3D/Welcome.html`

[3]From the Fornax Cluster Catalog (FCC) (Ferguson, 1989).

Chapter 2

Objectives

The aim of this work is to study the PNe spectra for four early-type galaxies of the Fornax cluster: FCC 153, FCC 167, FCC 170 and FCC 177[1] in order to obtain the LF, which relates the number of PNe present in the galaxy with their corresponding absolute magnitude of the [OIII] doublet. This function represents a well defined second indicator of distances because of the physics in the formation of PNe is the same in the most cases. Moreover, the differences in absolute magnitude are able to indicate the presence of different progenitor stellar populations: from blue-stragglers to intermediate mass stars or solar-mass stars.

On the other hand, in this work the kinematics of the PNe for the four galaxies is analysed in comparison with the kinematics of the stellar background in order to observe whether the both components are in agreement between each other or not. This result is able to show us discrepancies between the two components which could be due to different processes like: presence of outliers, false detections, decoupled components, external PNe, etc.

Lastly, we are going to compare the metallicity obtained for three of the four galaxies with the number of the detected PNe in order to obtain some clue about the formation and evolution of the PNe and their relation with the region in where they are hosted.

The chapter 3 is dedicated to the methodology: the extraction process of PNe spectra, how we determine the kinematics of the PNe, the estimation of the LF and the metallicity of these objects through the stellar background. We also explain the fitting modeling of the spectra and the estimation of the systemic velocity for each PNe. The results are described in chapter 4. Last, in chapter 5 we show our conclusions.

---

[1]FCC is the Fornax Cluster Catalog. The correspondence for this galaxies in other catalogs are, respectively: IC 1963, NGC 1380 , NGC 1380A and NGC 1381.

Chapter 3

Methodology

Both the LF and the kinematics of the PNe requires of the PNe spectra to be estimated. To obtain the spectra, we need to locate those sources which are PNe. This process of extraction requires to consider just the emission of these objects, due to the phenomenology that accompanies them. Once we have obtained the spectra, both the estimation of the kinematics and the LF may be studied.

In this chapter, we explain the methods used to obtain the kinematics of the PNe (and the stellar background) and their LF along with the estimation of metallicity in order to compare with the number of detected nebulae.

1. The MUSE data

The MUSE[1] is an integral field spectrograph placed in the Very Large Telescope (VLT), which operates in the visible wavelength range (between 4650 and 9300 Å) and is able to obtain the spectra received from a source and package it in each pixel of the camera. Thereby, we have one spectrum in each pixel which allows us to study the source in a whole wavelength range without the necessity of taking the images in different filters. Therefore, MUSE offers 3D data cubes which consist in two spatial coordinates x and y and one spectral coordinate λ in where the spectral information is codified.

Our data samples are plotted in Figure 3.1 in where each pixel represents 0.2 arcsecs in the MUSE Field of View (FoV). The images correspond to (from left to the right): FCC 153, FCC 167, FCC 170 and FCC 177. The images are the reconstruction for the wavelength range between 4900 Å and 5100 Å. The signal-to-noise varies from one pointing to another and the pointings which contain the galaxy centers have the highest signal-to-noise ratio.
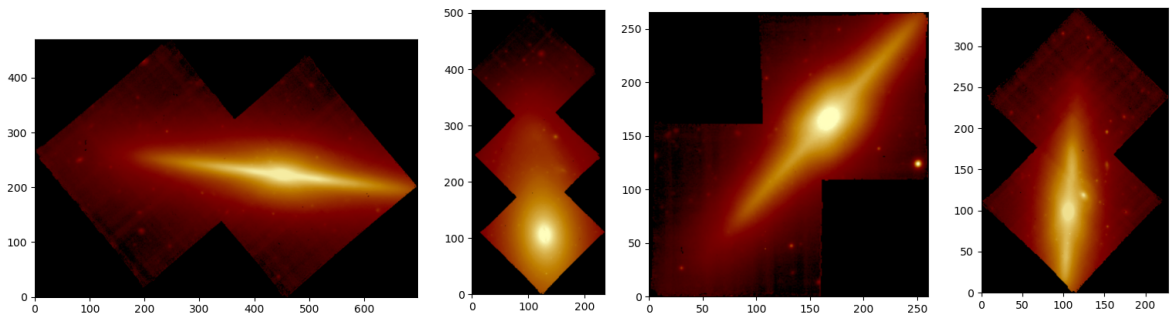
Figure 3.1: MUSE galaxy samples for the Fornax3D project from the left to the right: FCC 153, FCC 167, FCC 170 and FCC 177. The images result from the sum in wavelength between 4900 Å and 5100 Å to get just an image of the galaxies. Each pixel in the image corresponds to 0.2 arcsecs in the MUSE FoV.

As we can observe, all the samples are edge-on galaxies. This fact is crucial to determine the kinematics of the PNe because for face-on galaxies we are unable to measure the radial velocity of the constituents but

---

[1]The technical specifications are tabulated in `https://www.eso.org/sci/facilities/develop/instruments/muse.html`.

of the galaxy itself, so in this situation we cannot quantify the movement of individual PNe with respect to the galaxy.

2.   Spectra of the PNe

The spectrum emitted by PNe, as we said previously, is characterised by strong [OIII] doublet emission which is considerably greater in flux than the continuum[2]. To perform the analysis of the PNe, it is necessary to divide the contribution for each spectrum in its two components: stars and PNe. This process is typically applied to this kind of studies (Coccato et al., 2009; Pastorello et al., 2013; Sarzi et al., 2011) where the emission of the spectra is the object of analysis. In order to obtain the emission spectrum for each object, we need to subtract the continuum from our spectra. To measure the spectra of the PNe in different samples of galaxies, we need first to detect the PNe hosted in the corresponding galaxy. Once we have the different sources which are potential candidates to be PNe, it is necessary to filter each source attending to the shape of its spectrum, to the spatial distribution of the detected source, to the signal-to-noise of the sample and to the receding velocity of each detection[3]. The PNe are point sources which appear as extended sources due to the Point Spread Function (PSF) of the instrument, which describes the response of an optical system to a point source. So it would be expected to observe various bright pixels around a centroid which are brighter than the adjacent area. With respect to the spectrum, the observed 5007 line is approximately three times brighter than the 4959 line (Bowen, 1927), except for regions with high amount of dust (Kwok, 2007) in where the 4959 may be hidden.

The spectrum we received from a PN is shifted due to both the cosmological expansion and the peculiar velocity of the object with respect to us. These quantities may be obtained from the Hubble's law (Binney and Merrifield, 1998):

$$v_{rad} = H_0 d + v_{pec}, \tag{3.1}$$

where v_{rad} is the radial velocity of the galaxy, H_0 the Hubble's constant, d the proper distance to the galaxy and v_{pec} the peculiar velocity of the galaxy which represents an anisotropy from the Hubble's law.

Due both the peculiar movement of the galaxy and the cosmological expansion, the [OIII] is redshifted to higher wavelengths. The total redshift is given by (Binney and Merrifield, 1998):

$$z = z_{cos} + z_{pec}, \tag{3.2}$$

where z_{cos} is the cosmological redshift due to the expansion and z_{pec} is the peculiar redshift due to the systemic velocity of the galaxy and its constituents. In the case that concerns, the Fornax cluster is in the low redshift regime ($z << 1$), so the expression for the redshift acquires the form:

$$z = \frac{\Delta\lambda}{\lambda_{em}} \tag{3.3}$$

where $\Delta\lambda = \lambda_{obs} - \lambda_{em}$ is the difference between the wavelength observed and the wavelength emitted.

In edge-on galaxies, the objects approach or recede from us affecting to the redshift of the spectrum, and so this effect permits to measure the kinematics of the properly objects.

The redshift of the galaxy gives to us the information needed to obtain the peculiar velocity for each PN using the expression (3.3). In practice, the redshift we quantify when we estimate the spectra of a galaxy is the total redshift given by expression (3.2).

---

[2]Usually around two orders of magnitude higher.

[3]High velocity sources are not properly of the host galaxy and may be external objects which are able to be cataloged.
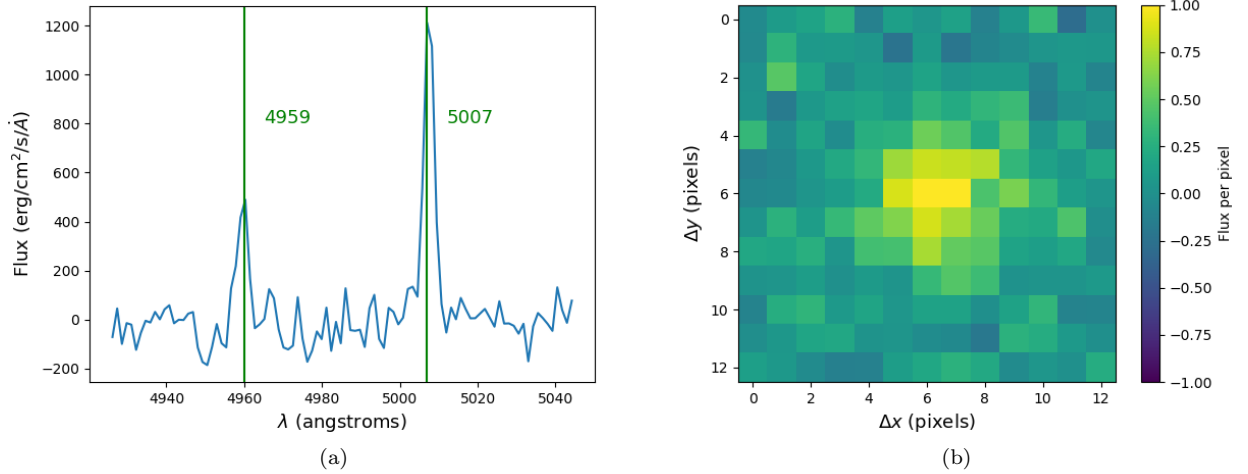
Figure 3.2: The spectrum of a planetary nebula detected in FCC 170 (figure (a)) along with its correspondent image of the detection (figure (b)). The aperture considered to this detection is a square window of 13×13 pixels around the centroid of the detection and each pixel represents 0.2 arcsecs in the MUSE FoV. In this case, the spectrum is the result of adding up each detected spectrum for each pixel of the aperture. The green lines indicate the [OIII] doublet in Å. The flux per pixel in the spatial distribution is normalized to unity to avoid high differences between the [OIII] peak and the continuum.

Figure 3.2 shows the typical shape of spectrum of a PN with the doublet [OIII] line perfectly visible along with the image of the detection in a square aperture of 13×13 pixels. The spectrum is the result of summing each spectrum for each pixel. As we can observe, the 5007 line is roughly three times greater than the 4959 line. For the spatial distribution, it is possible to observe the source from which we obtain a high amount of counts per pixel around the centroid of the source, due to the effect of the PSF. The flux per pixel is normalized to unity in order to smooth the distribution along the whole window to avoid great differences between the pixels with high positive flux and pixels with high negative flux.

2.1.   Extraction process

The first step in the extraction process is to subtract the continuum of our galaxies to get only emission spectra.

In order to proceed with this task, we have rescaled the spectra with SSP models from different libraries. In our case, we have used the MILES library described in Vazdekis et al. (2010). With these templates, we fit the spectra of the galaxies for each bin using the code $pPXF$[4]. The binning of the galaxy spectra is performed through the Voronoi binning method described in Cappellari (2009). The $pPXF$ code estimates the kinematics parameters (velocity, velocity dispersion and Gauss-Hermite coefficients) along the Line of Sight (LoS) applying SSP to each bin. Moreover the algorithm provides us the fits of the original spectra with which we can subtract the continuum from the original cube.

---

[4]The $pPXF$ code is a program to extract the kinematics of the stars developed by Michelle Cappellari and Eric Emsellem through the Penalized-Pixel Fitting method described in Cappellari and Emsellem (2004).
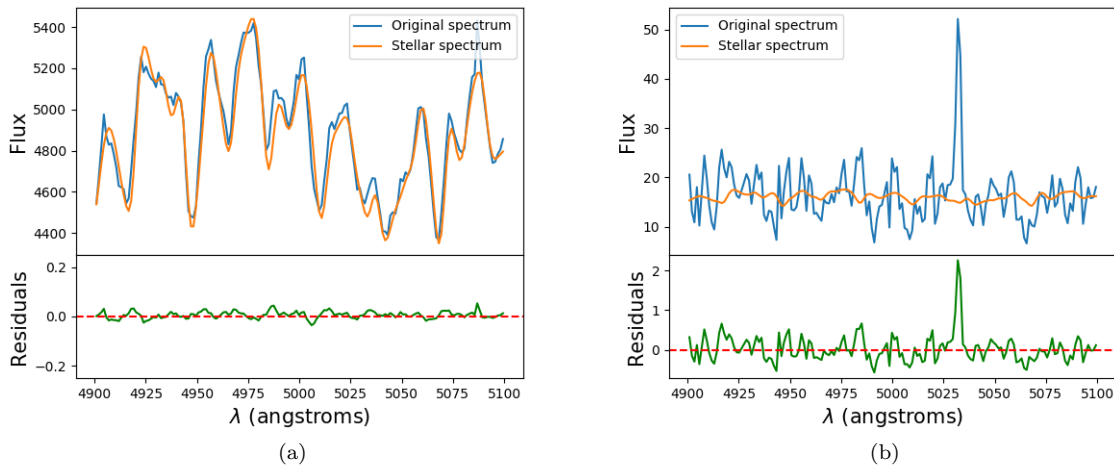
Figure 3.3: Original spectra versus fitting stellar spectra for central region (a) and for a PNe dominated region (b). The spectra are obtained from FCC 170. The stellar spectra are obtained using the code *pPXF* which fits the SSP models with the spectra of the galaxy. The plots below the spectra are the residuals resulting of extract the stellar spectra of the original spectra.

In Figure 3.3 we show the comparison between the spectrum received from the central region for the original MUSE spectrum, and the stellar spectrum resulting from applying *pPXF* to the spectra of the galaxy. In figure (a) we can observe the comparison of a spectrum of the central region and its stellar best fit. Figure (b) shows the spectrum received from a PNe dominated region and its best stellar fit. The plots below the comparison show the resulting residuals from subtract the stellar spectra to the original spectra. As we can see, the residuals for the central region are below the 0.05, and below the 0.5 for the PNe dominated region except for the emission line in Figure (b) which is in fact the shifted 5007 line. This rescaling allows us to measure the emission lines over the continuum for those regions which we could not see without it. On the other hand, the rescale smoothes the light distribution between the brightest zones and the faintest ones and do not affect to the emission regions. Generally the bulge and the disk are much brighter than the halo, so with the rescale we homogenize the amount of light received from all the regions.

Due to our data consists of many pointings for each galaxy, the PSF acquires different values for each one, so it is important to work independently with each pointing. In the overlapping region, many sources detected may coincide in both pointings, so it is necessary to consider this detections just for the pointing with better signal-to-noise (typically the central pointing). Therefore, the extraction process must be done individually for each pointing and then combine them taking a common source between them in order to get the offset.

With the emission cube, the next step is to cut in wavelength around the [OIII] doublet. The wavelength range has to be wide enough to preserve the typical Gaussian shape of the emission lines and smaller enough so that the other emission lines do not fall within the spectrum. It is crucial to split the spectra in a window in which the [OIII] doublet is contained in order to see the presence of the two lines. With this consideration we will get a [OIII] emission cube which we can sum in wavelength in order to get just an image where the possible PNe are shown.
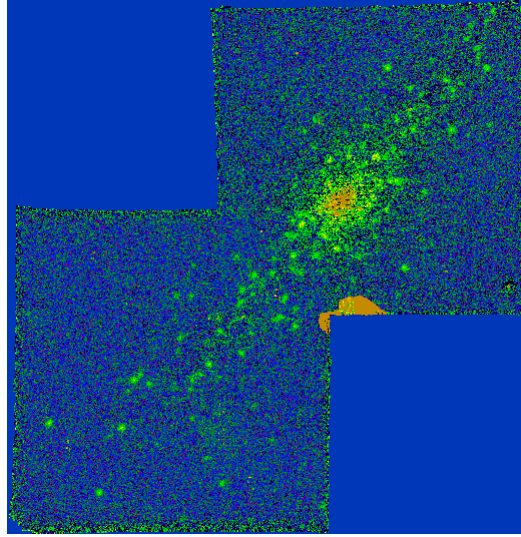
Figure 3.4: Image of FCC 170 around the shifted 5007 line. The image is obtained subtracting the continuum of the original data cube and then, summing in wavelength around the shifted 5007 line.

In Figure 3.4 we can observe the resulting image around the shifted 5007 line for FCC 170 after subtracting the continuum. Then, with the continuum subtracted, we sum in wavelength around the shifted 5007 line to obtain an image with the zones which emit in this wavelength. With this image, we can detect the different sources which are susceptible to be PNe.

Detection of PNe

Once we have the image corresponding to the sum of all spectral pixels around the shifted 5007 line, we have used the software *SExtractor* to detect the different sources in an area of 5 pixels around the centroid[5] (Merrett et al., 2006). *SExtractor* generates a table with the coordinates for each detected source which we have to analyse in order to distinguish between PNe and false detections and/or outliers.

The detection method is similar to the process applied by Merrett et al. (2006); Pastorello et al. (2013); Sarzi et al. (2011), where the [OIII] doublet serves as indicator for those pixels where could have a potential candidate to be a PN. In our study, we have selected a window wide enough around the shifted [OIII] doublet to detect the Gaussian shape of the emission line and to be able to distinguish the background of the spectra. Then, we apply a Gaussian fit to the spectrum given by:

$$g(\lambda) = \frac{A}{\sqrt{2\pi}\sigma} e^{-\frac{(\lambda - \lambda_0)^2}{2\sigma^2}}, \tag{3.4}$$

where A is the normalization constant which must coincide with the value of shifted 5007 line, σ is the standard deviation of the [OIII] lines which typically adopt the value of $\sigma = 1.19$ which comes from the MUSE spectra resolution. λ_0 are the corresponding wavelengths to the [OIII] lines. If we apply this fit for the [OIII] doublet we obtain:

$$g_{OIII}(\lambda) = \frac{A_{OIII}}{\sqrt{2\pi}\sigma} \left[\frac{1}{3} e^{-\frac{(\lambda - 4959)^2}{2\sigma^2}} + e^{-\frac{(\lambda - 5007)^2}{2\sigma^2}} \right], \tag{3.5}$$

which implies the two lines of the doublet and the condition of $A_{OIII}/3$ for the amplitude of the 4959 line with respect to the 5007 line. With the fit of the sources around the [OIII] line, we can distinguish better the sources which may be good candidates to be considered as PNe.

---

[5]A planetary nebula is a point source observed as an extended source due to the PSF. We have to consider a source within an annular aperture not only for simplicity, but also to get a well measure of the spectrum around the centroid. Focusing around the centroid allows us to reduce as much as possible the noise of the background for the aperture considered.

Extracting the spectra

Once we have the data reduced and the maps with the PNe obtained, we can estimate the spectra for each PN considering an annular ring of roughly 1.4 arcsecs. For MUSE, 0.2 arcsecs = 1 pixel, so we have to consider over 7 pixels of aperture around the centroid of the sources detected by *SExtractor*. Adding up the spectrum contained for each pixel we obtain the total spectrum for each PN.

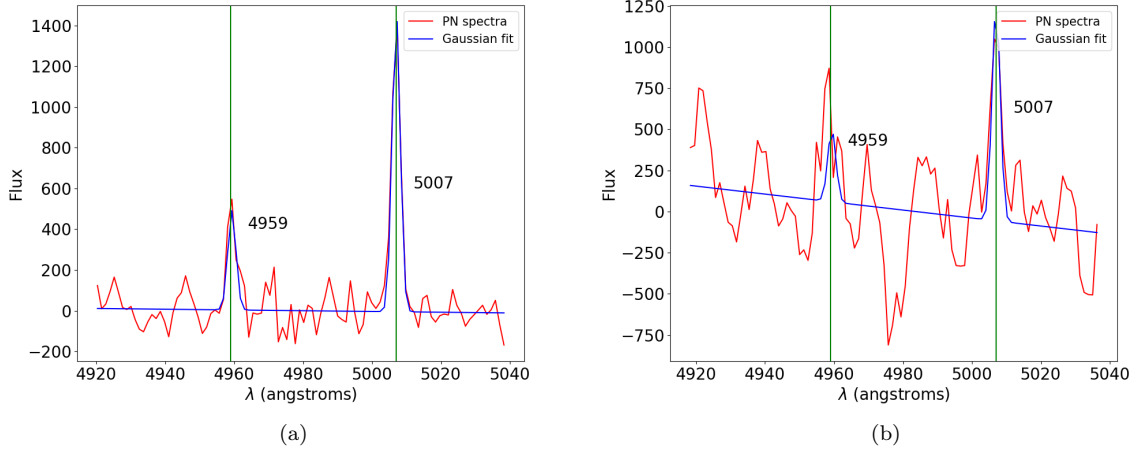(a)   (b)

Figure 3.5: Spectra of two sources detected in FCC 167 with *SExtractor* with the Gaussian fits for the [OIII] lines which conforms the doublet (red and green lines). The spectra are obtained through the sum of the individual spectra for each pixel which compound the annular aperture. The spectra is shifted due to cosmological redshift and the peculiar velocity of the sources. The Gaussian fits are given by equation 3.5 with $\sigma = 1.19$ defined by the MUSE spectral resolution. Figure (a) shows a well defined PNe while in figure (b) we show an example of a bad detection in where the fit and the spectra are not well fitted.

In Figure 3.5 we can see the Gaussian fitting of two spectra obtained as a result of the sum of the individual spectra for the pixels which conform the annular aperture for two different sources present in FCC 167. In figure (a), we can observe a well defined [OIII] doublet which coincides with the Gaussian fits and low level of noise. These two features confirm this source is in fact a planetary nebula. However, for figure (b) we are in a typical situation of a spectrum for which the presence of 5007 line is clear but not for 4959 line. On the other hand, the high level of noise contaminates the sample making this analysis inadequate to consider this source as PN.

Taking into account the PSF for extraction we are able to obtain the total flux of the PNe, and consequently the absolute magnitude. Knowing the PSF we can fit a Moffat profile to a bright star which falls within the FoV of the instrument. The expression for a typical 2D Moffat profile is given by:

$$F_{OIII}(x, y) = A_{OIII} \left(1 + \frac{(x - x_0)^2 + (y - y_0)^2}{\gamma^2} \right)^{-\alpha}, \tag{3.6}$$

being A_{OIII} the amplitude of the profile, x and y the spatial coordinates, x_0 and y_0 the coordinates of the source center and α and γ are the PSF parameters. This expression describes the ideal image in flux which we would obtain from a PN in the noise free situation. Through the Moffat profile, we are able to model the shape of an extended source like a PN for the ideal scenario in which we would just have the source and the PSF of the instrument.

In the absence of bright star in the FoV we can model the PSF through the brightest PNe in the galaxy. We have selected the six brightest PNe[6] detected in the four galaxies. A similar method to obtain the PSF from a sample through Moffat fitting of the sources is used in (Merrett et al., 2006) in which the FWHM for each source is estimated through this method.

---

[6]It is necessary to select a modest amount of objects in order to estimate the average value between them and because of this six objects will have more similar properties between them than from a sample of many PNe for which many of them will have evolved and the luminosity of them will have changed.

Fitting Gaussian 1D distributions to the spectra for this bright PNe we can characterise the parameters α and γ of the Moffat profile in order to get the PSF of the galaxy. Indeed, we begin with and arbitrary values for A_{OIII}, α and γ. Then, we minimize both the spatial distribution respect to the Moffat 2D model and the spectrum respect to the Gaussian 1D. Both models are related by the amplitude A_{OIII} through the relation:

$$A_{OIII} = \frac{F_{OIII}(x,y)}{\sqrt{2\pi}\sigma},\tag{3.7}$$

with $\sigma = 1.19$ for the [OIII] lines. Minimizing the difference between the spectra and the Gaussian 1D fits provides us the values not just for A_{OIII} but also for α and γ. With these values, we recover the PSF of the instrument for each galaxy.

Once we have the PSF parameters we apply the fits for all detections in order to obtain the amplitude of the Moffat model, and then, with the amplitude of the model we obtain the flux for each PN, and consequently the absolute magnitude.
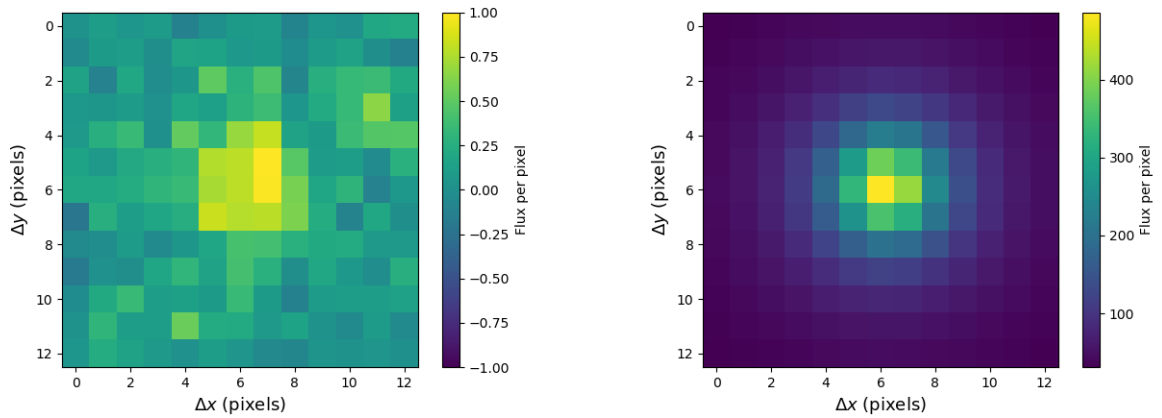

Figure 3.6: Moffat 2D model of a PN detected for FCC 167. The flux per pixel are normalized to unity in the case of the spatial distribution in order to smooth it. This consideration is not necessary to be applied for the Moffat model due to the absence of noise. The figure (a) represents the amplitude distribution of the PN detected in a square window of 13×13 pixels. The figure (b) shows the resulting Moffat model for the PN. In the Moffat model each pixel is the amplitude of the [OIII] doublet given by equation (3.7). To obtain the model, we minimize the difference between the Gaussian fit and the spectrum in order to obtain A_{OIII} and then α and γ applying the Moffat model for that amplitude.

In Figure 3.6 we can observe a PN detected in FCC 167 with the correspondent Moffat 2D model applied to this detection in order to get the PSF parameters of this galaxy.

To obtain the model, we minimize the difference between the Gaussian fit and the spectrum of the PN in order to obtain the amplitude A_{OIII}. Silmutaneously, we applied that amplitude to our Moffat 2D to get the coefficients α and γ. Taking the resulting Moffat profile we have the flux of the [OIII] doublet for each pixel, and summing it we can estimate the total flux of the [OIII] doublet for the PN.

We have to take into account the number of pixels chosen for the aperture. The larger the aperture, the greater the signal obtained but also the noise. We have to take care with the size considered for the aperture, trying to get a compromise between good signal for the region selected and reasonable level of noise which does not contaminate the sample. In principle, the width of the aperture varies from one galaxy to another.

2.2. Determining the velocity of the PNe

The fit of the PNe spectra is a key path to get the systemic velocity of the PNe as well as determine if the sources detected by *SExtractor* may be considered as PNe or another kind of object, as stars, death pixels, external sources, or others. As we already said, fitting Gaussian distributions to [OIII] doublet we can discriminate those sources which are potential candidate to be PNe from those which not. Moreover, the

centroid of the 5007 line provides a good indicator of the redshift of the spectrum, and consequently, of the velocity. Therefore, knew the position of the shifted 5007 line with respect to the line in restframe, knew the velocity of the planetary nebula.

On the other hand, the kinematics represents another key to be sure that our detections are PNe: those objects with velocities many times greater than the host galaxy do not belong to the galaxy itself and must be discarded of the catalog[7]. For this reason, the accurate in the measure of the peak for [OIII] line is crucial in order to not include those "false detections" with velocities absurdly high (or low).

Once we have filtered all sources and discarded those which do not fulfill the previous conditions, we would have the spectra for all the detected PNe. To proceed with this study, we use the definition of redshift given by equation (3.3) and the relation between it and velocity Binney and Merrifield (1998):

$$v = cz. \tag{3.8}$$

with $c = 299,792.458$ km/s is the speed of light. Hence:

$$v = c \left[\frac{\lambda_{OIII}^{(obs)}}{\lambda_{OIII}^{(em)}} - 1 \right], \tag{3.9}$$

so, knowing the position of the [OIII] centroid[8] for each PN, we can obtain the systemic velocity of the PN with respect to us. Those objects with velocity greater than 350 km/s (in absolute value) with respect to the center of the galaxy may be external PNe which proceed from the cluster instead of the own galaxy (Coccato et al., 2009). With all of this ingredients, we are able to analyse both the kinematics and the LF of the PNe for all galaxies.

3.   PNe kinematics and the stellar background

Once we have determined the kinematics of the PNe for our resulting catalog, we can proceed to compare it with the stellar background in order to observe any similarities between the two type of objects. In order to compare both components, we refer the velocity to the center of the galaxy[9]. For PNe we modify the equation (3.9):

$$v_{PN} = c \left[\frac{\lambda_{OIII}^{(obs)}}{\lambda_{OIII}^{(em)}} - 1 \right] - \bar{v}_{PN}(r < 10), \tag{3.10}$$

with in this case, $\bar{v}_{PN}(r < 10)$ are the mean velocity (or the systemic) for nebulae considering those PNe which are in a region of $r < 10$ arcsecs. This consideration provides us a good approximation to the central velocity of the galaxy, in this case for PNe. It is necessary that in the considered region must fall the same number of objects with positive receding velocities (with respect to us) that with negative receding velocities to obtain a well determination of the mean velocity. Subtracting this quantity to the individual velocity of each PN, we obtain the velocity referred to the galactic centre.

For stars, we proceed in the same way:

$$v_{\star} = c \left[\frac{\lambda^{(obs)}}{\lambda^{(em)}} - 1 \right] - \bar{v}_{\star}(r < 10), \tag{3.11}$$

the only difference is that here the redshift is analysed along all the spectrum of the stars. In this case, the redshift may be obtained with no more than identify a known absorption line in the spectra of the stars. For it, we have used the *pPXF* code to obtain the kinematics of them in order to compare with the PNe.

It is important to study the ratio between the velocity of PNe and the velocity dispersion of these ones. Velocity dispersion may not be obtain directly from PNe, because these sources are isolated one from each other, and in the majority of the cases we will not have many of these objects in consecutive pixels. In fact, we can obtain the velocity dispersion assuming that the PNe possess the same velocity dispersion as the stellar background behind them (along the LoS). So in this case, we can calculate the dispersion by simply obtaining for the bin of the stellar background nearest to each PNe. This approximation is valid to first order.

---

[7]We are focusing just for objects which belong to the own galaxy, and not to objects which proceed from the cluster and fall within the galaxy.

[8]In this case, when we said [OIII] we are referring to the 5007 line.

[9]This condition is not crucial, but it makes the study easier.

4. The Planetary Nebulae Luminosity Function

With the total flux of the [OIII] doublet obtained through the PSF of the instrument, we are available to calculate the magnitudes of the PNe. In order to estimate it, we applied the relation between the flux of the [OIII] doublet and the apparent magnitude given by the expression (Ciardullo et al., 2004):

$$m_{5007} = -2.5 \log F_{5007} - 13.74, \tag{3.12}$$

where the flux is given in erg cm^{-2} s^{-1} Å^{-1}. With the apparent magnitude we are available to calculate the absolute magnitude of the PNe taking this value and the distance to the host galaxy[10]. The distance to various galaxies of the Fornax cluster are measured by Blakeslee et al. (2009) through estimations of surface fluctuations obtained with the Hubble Space Telescope (HST). With these measures of distance modulus we can obtain the absolute magnitude for each PN.

Galaxy	$(\mathbf{m} - \mathbf{M})$	Hubble type	$\mathbf{R_{eff}}$ (arcsec)
FCC 153	31.588 ± 0.071	Sab	26.2
FCC 167	31.632 ± 0.075	S0/a	72.7
FCC 170	31.705 ± 0.076	S0	17.97
FCC 177	31.509 ± 0.065	S0a	37.8

Table 3.1: Properties of FCC 153, FCC 167, FCC 170 and FCC 177. The distance modulus and its errors has been extracted from (Blakeslee et al., 2009). The effective radii tabulated are extracted from Iodice et al. private communication.

In Table 3.1 figures different data of the four galaxies of study. The modulus distance $(m - M)$ is extracted from Blakeslee et al. (2009) whether the effective radii are extracted from Iodice et al. private communication. Once we have obtained the absolute magnitude, we are able to estimate the LF for the expression given by Ciardullo et al. (1989):

$$N(M) \propto e^{0.307 M_{5007}} \left[1 - e^{3(M_{5007}^{\star} - M_{5007})} \right], \tag{3.13}$$

where $M_{5007}^{\star}$ is the absolute magnitude of the brightest PN which represents a cut-off in the LF. The amplitude of this law is an arbitrary factor which depends on the galaxy and the shape of the PNe distribution with respect to M_{5007} but it does not alter the shape of the standard law.

Once we have the values of the M_{5007} for each PN we proceed to compare the distribution of this values with the number of PNe for each galaxy. This process is performed through a histogram which relates the binned absolute magnitude with the number of PNe for each bin. The number of bins for it can be chosen after fit the data with the standard law (Rodríguez-González et al., 2015), so the process is relatively random. Indeed, both the number of bins and the initial position for the bins as well as the bin size are free parameters, which must be chosen in order to fit with the standard law (Rodríguez-González et al., 2015).

With respect to the incompleteness of the PNe, many studies restrict the analysis from the cut-off of the LF to the peak of it where function dips. This procedure is useful for those galaxies where star formation is been produced (Rodríguez-González et al., 2015).

4.1. Metallicity of the samples and absolute magnitude of the PNe

The number of the PNe are intrinsically related to the metallicity of the host galaxy (Buzzoni et al., 2006; Sarzi et al., 2011), and this fact could impact in the number of brightest PNe (Pastorello et al., 2013) and furthermore in the number of central PNe stars (Rosenfield et al., 2012). Otherwise, the relation between the number of PNe and the metallicity may show us the differences in mass between the halo and the disk through the parameter $< Z >$ which represents the luminosity weighted metallicity for the stellar regions probed by the PNe and defined as follows:

$$< Z >= \frac{\sum_i Z_i F_i}{\sum_i F_i}, \tag{3.14}$$

---

[10]The distance between the PN and the galaxy are negligible versus the distance from the observer to the galaxy. We adopt the criterion that all the PNe are at the same distance from us.

where Z_i is the metallicity of the stars/PNe with respect to the Sun given by $Z_i = \log\left([M/H]/[M/H]_\odot\right)$. F_i is the flux emitted by the PNe or the stellar background. The ratio consists in the sum of the product between the metallicity per flux, and the sum of the flux. This parameter weights the influence of the metallicity against the flux of the objects for each galaxy. To estimate the metallicity of the stellar background, we have appealed to *pPXF* in order to estimate it for each bin. The process is described in Kuntschner et al. (2010) where they obtain the weights of the stellar spectra fitting to multiply them with the given metallicity for each SSP model. With the metallicity calculated, we have assumed that the PNe which fall in a concrete bin have the same value for metallicity than the stars for that bin. This consideration is a first approximation valid enough for our purpose.

4.2. Summary

After obtaining the PSF for the four galaxies, we can summarize the extraction process of both velocity and absolute magnitude of the PNe in the next items:

1. Rescale the original MUSE cube with stellar templates in order to subtract the continuum.

2. Split the emission cube to wavelength range between 4950 and 5050 Å in order to get a cube which contains mainly the [OIII] doublet and sum around the shifted 5007 line to get just an image of the [OIII] brightest line.

3. Run *SExtractor* on the [OIII] image to detect many sources which are able to be candidates to PNe.

4. Fit Gaussians to [OIII] doublet lines and observe to the shape of the spectrum for the different sources detected and discard those sources which do not well adjust to Gaussian fits.

5. Fit Moffat 2D profiles to spatial distribution of the remaining sources in order to obtain a measure in flux of the [OIII] doublet for each PN.

6. Finally, measure the velocity and absolute magnitude of the shifted 5007 line.

Through this steps, we are in conditions to obtain both the kinematics and luminosity function of the four samples of galaxies.

Chapter 4

Results

In this chapter, we show the results for the different aims established: the detection of the PNe for the four ETGs, the LF compared with the standard law and the kinematics of the PNe compared with the stellar background.

1. Detections and spectra of PNe

Through the image of the galaxies for the 5007 line, we are able to observe all those regions in which there is emission of this transition. It is necessary to take into account that the presence of this emission line is not a ratification of the existence of a planetary nebula in the region, because there are sources like Lyman-α galaxies at redshift $z \sim 3$ or OII at $z \sim 0.347$ which emit in the same range of wavelengths as [OIII] (Spiniello et al., 2018). Besides, the 4959 line permits to quickly distinguish between fake emitters and true PNe.
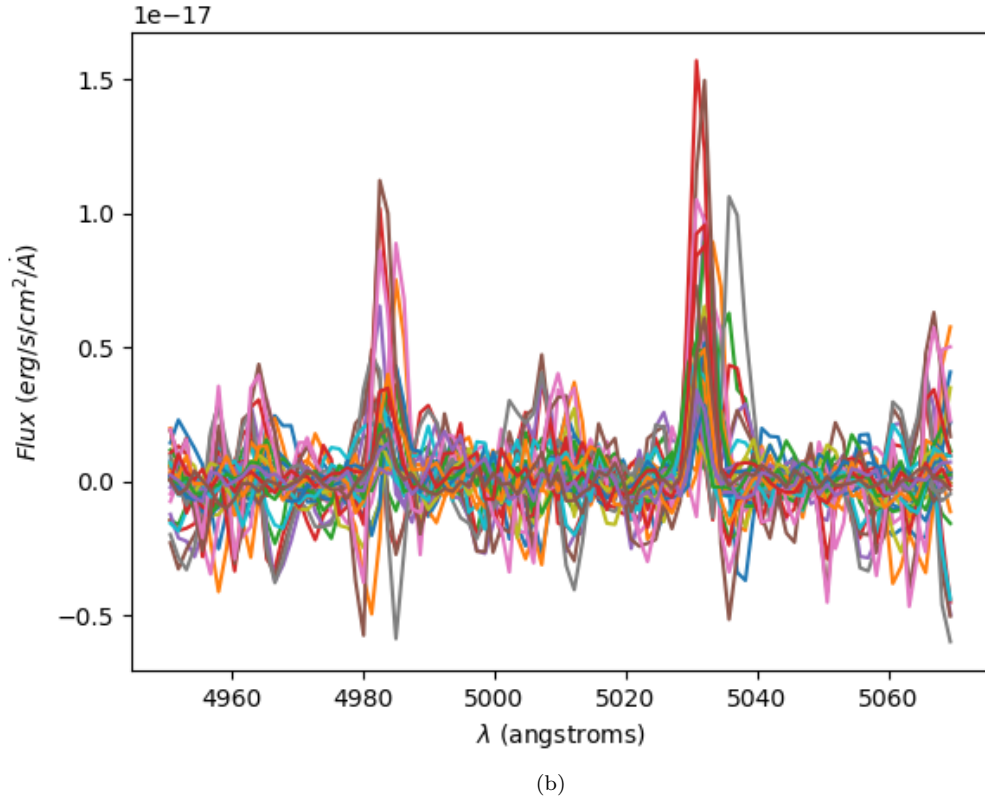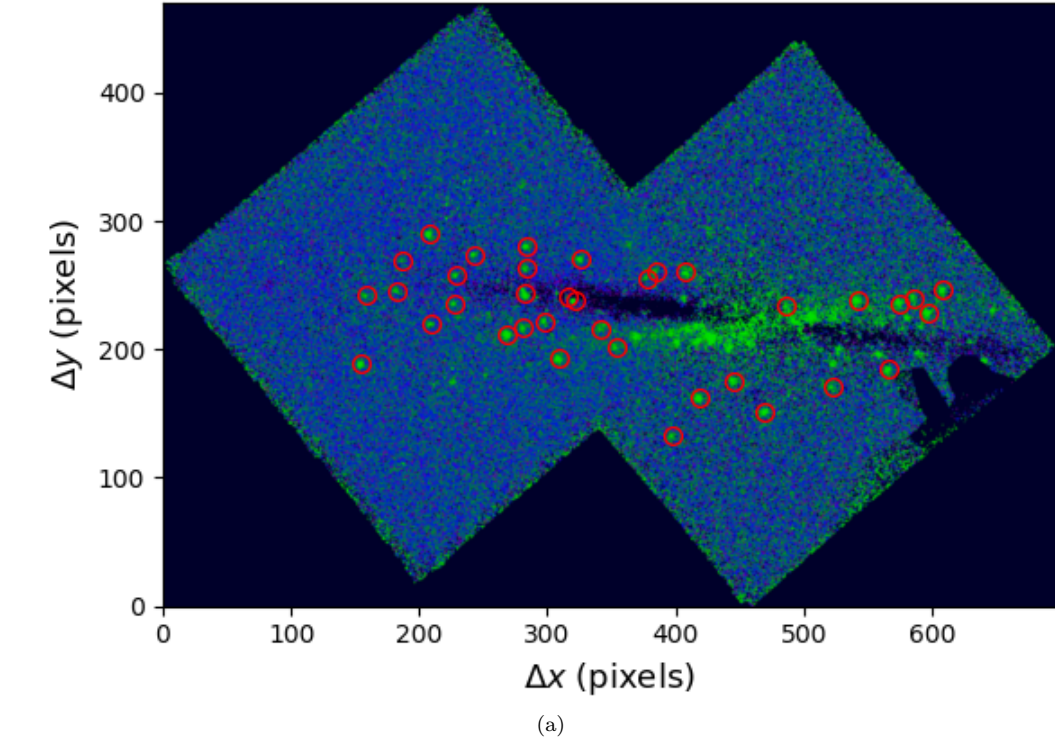
(a)

(b)

Figure 4.1: FCC 153 around the [OIII] window (a) along with the spectra of the detected PNe (b). The estimation of the spectra is obtained summing all the spectra contained in a window of 11×11 pixels around the centroid of the sources. There are 36 detections in this galaxy

(a)

(b)

Figure 4.2: FCC 167 around the [OIII] window (a) along with the spectra of the detected PNe (b). The detected PNe are marked with red dots. The estimation of the spectra is obtained summing all the spectra contained in a window of 11×11 pixels around the centroid of the sources. For the map of detections, there are 61 detected PNe.
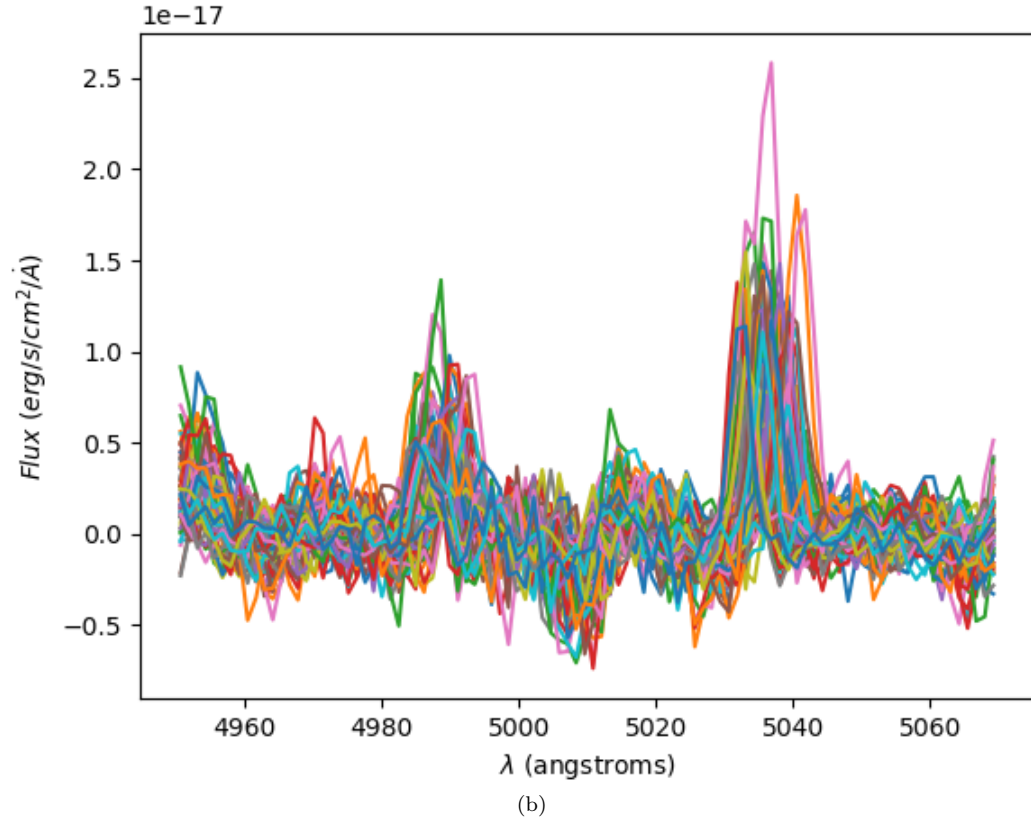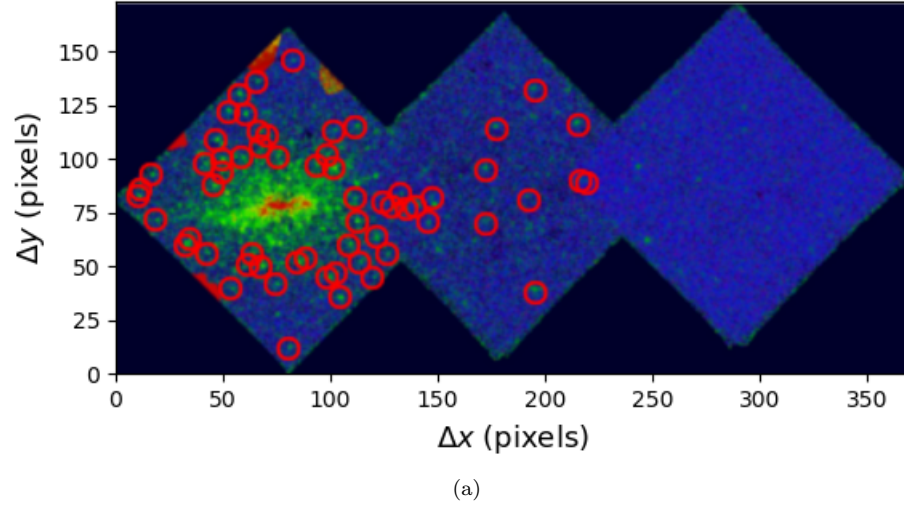
(a)

(b)

Figure 4.3: FCC 170 around the [OIII] window (a) along with the spectra of the detected PNe (b). The detected PNe are marked with red dots. The estimation of the spectra is obtained summing all the spectra contained in a window of 11×11 pixels around the centroid of the sources. There are 41 detected PNe.
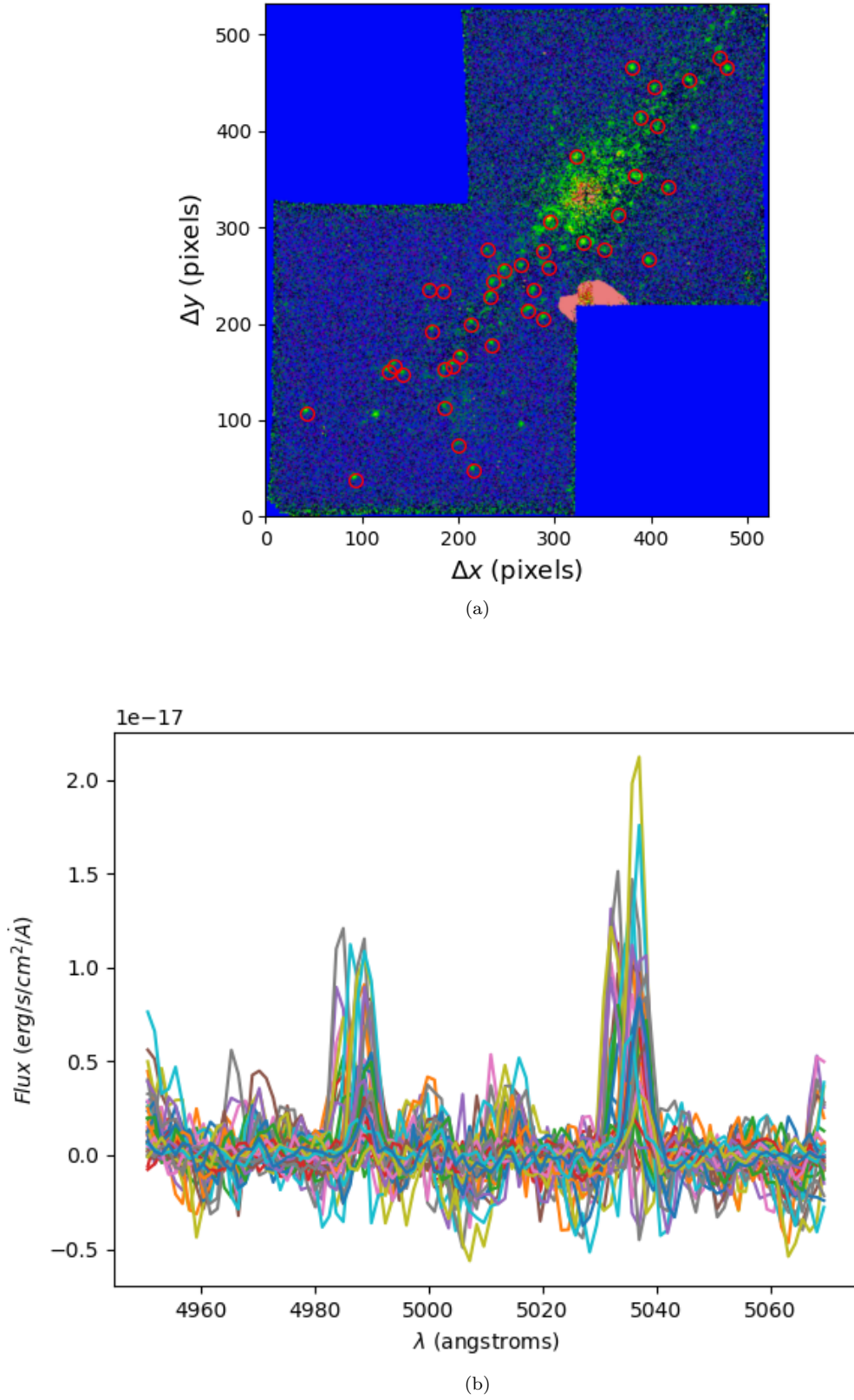
(a)

(b)
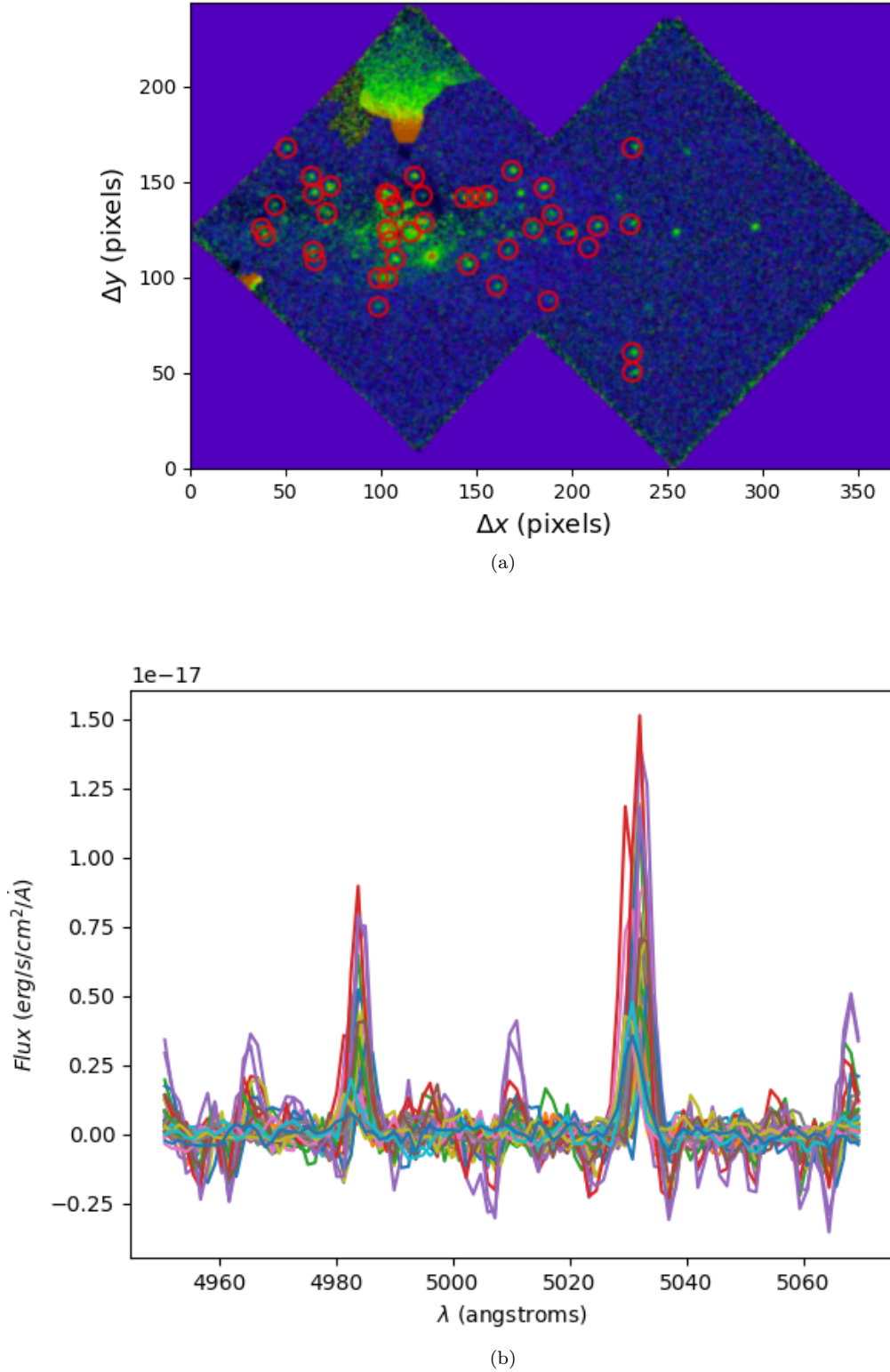
Figure 4.4: FCC 177 around the [OIII] window (a) along with the spectra of the detected PNe (b). The detected PNe are marked with red dots. The estimation of the spectra is obtained summing all the spectra contained in a window of 8×8 pixels around the centroid of the sources. In this case, the total number of detected PNe is 41.

Figures 4.1-4.4 show the maps of [OIII] for the four galaxies (figures (a)) with the detected PNe represented with red circles. On the other hand, the figures (b) represent the spectra for all detected PNe. The spectra

are obtained summing the spectra of all the pixels in a square windows centered in the sources. This window depends on the signal-to-noise for each galaxy and in the values of the resulting PSF. For FCC 153, FCC 167 and FCC 170 the windows considered have a width of 11×11 pixels except for FCC 177 which the size of the window is 8×8 pixels. The detections which conform the resulting spectra in figures 4.1-4.4 are tabulated in the appendices 1-4. The number of detections for each galaxy is: 36, 61, 41 and 41; for FCC 153, FCC 167, FCC 170 and FCC 177 respectively. As we can observe, the [OIII] doublet is perfectly visible in the four compilation of spectra. Respect to the noise level, this varies from one galaxy to other due to the width of the window considered in the estimation of the spectra.

The distribution in the PNe is practically symmetric for FCC 167 and FCC 177, and there are certain inhomogeneities for FCC 153 and FCC 170 for which we have more detections in one side of the disk than in the other. For instance, in FCC 170 (Figure 4.3), the galaxy is not centered between the two pointings, due to this fact, the number of PNe is greater in the left side, so this particularly distribution may influence in the kinematics of both the PNe and the stellar background due to the geometry of the image.

For FCC 153, there is a blackened band along the disk in where we could not detect any PNe. Maybe, this result could have been produced due to the rescale of the spectra when we subtract the continuum. In this region, the level of signal is really low and it is essentially noise. This effect is due to the presence of dust in the disk which produces the extinction of the stellar light along the LoS.

2. Kinematics of the PNe

With the centroid of the shifted 5007 line we are able to determine the redshift for each individual nebula, and in this way, we can determine the velocities of the nebulae with respect to the observer. In this section, we show the results of the kinematics of the two components: PNe and stellar background; as well as the resulting analysis for these results.

2.1. Analysis of the two components: stars vs PNe

The error in the velocity of PNe we have considered is of the order of 10% of the v_{sys}, which corresponds to around 10 km/s. This error is in the interval between $10 - 40$ km/s, similiar to different studies (Pulsoni et al., 2017).
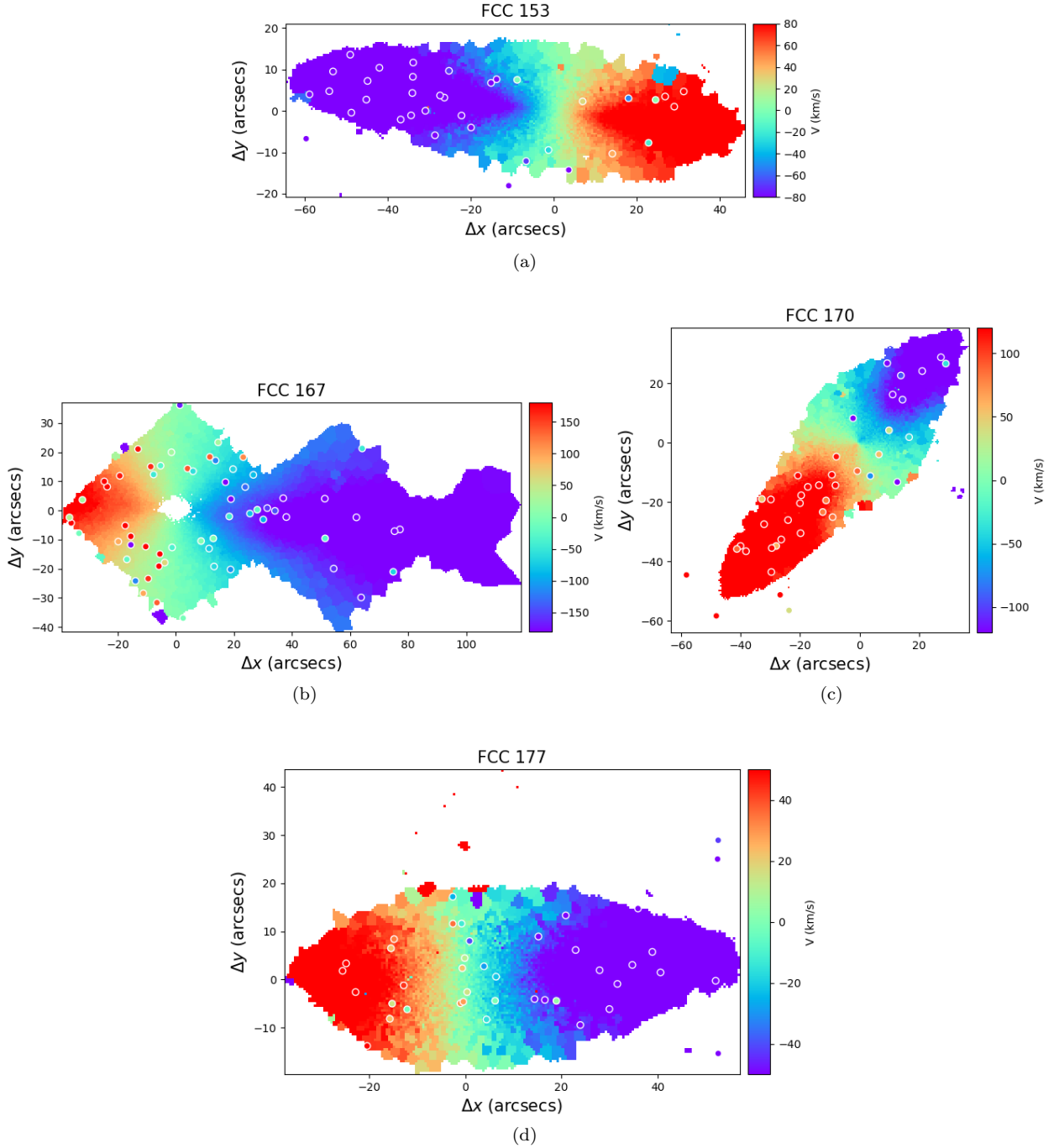
Figure 4.5: Kinematics maps of the stars and PNe. Figure (a): FCC 153. Figure (b): FCC 167. Figure (c): FCC 170. Figure (d): FCC 177. The dots represent the position of detected PNe with their correspondent value for the velocity along the LoS. The velocity are referred to the center of the galaxies for both stars and PNe.

In Figure 4.5 we can observe the kinematics of the stars and PNe for the four galaxies along the LoS: FCC 153 in figure (a), FCC 167 in figure (b), FCC 170 (c) and FCC 177 for the figure (d). The dots represent the kinematics of the PNe measured through the centroid of the shifted 5007 line. As we can observe, there is a good agreement between the kinematics of the PNe and the kinematics of the stellar background for FCC 170 and FCC 177. Both FCC 153 and FCC 167 present discrepancies between the velocity of the two components overall for the disk of 153 and for the center of 167. However, the differences in velocity between PNe and stars do not differ in more than 100 km/s, so in general terms, the PNe are capable to describe the movement of the stars in the host galaxies.

	v_{sys} (km/s)		Redshift		$v_{PNe}/v_{\star}$
Galaxy	**Stars**	**PNe**	**Stars**	**PNe**	
FCC 153	1627 ± 10	1593 ± 10	$(5.42 \pm 0.03) \times 10^{-3}$	$(5.32 \pm 0.03) \times 10^{-3}$	0.98
FCC 167	1862 ± 10	1763 ± 10	$(6.21 \pm 0.03) \times 10^{-3}$	$(5.88 \pm 0.03) \times 10^{-3}$	0.95
FCC 170	1735 ± 10	1666 ± 10	$(5.79 \pm 0.03) \times 10^{-3}$	$(5.56 \pm 0.03) \times 10^{-3}$	0.94
FCC 177	1574 ± 10	1514 ± 10	$(5.25 \pm 0.03) \times 10^{-3}$	$(5.05 \pm 0.03) \times 10^{-3}$	0.96

Table 4.1: Systemic velocity and redshift of the galaxies estimated through the PNe and the stellar background. The velocities are with respect to the observer. The estimation of redshift is given by the expression (3.8) for both components. The last column shows the ratio between the systemic velocity of the PNe and the systemic velocity of the stars. The error in redshift is given by the propagation of errors in the expression (3.8) with an uncertainty in velocity of 10 km/s.

The Table 4.1 contains the systemic velocity and redshift of the galaxies estimated through the PNe and the stellar background. Moreover, we have calculated the ratio between the systemic velocity of the PNe and the systemic velocity of the stars. These velocities are with respect to the observer. The error in redshift is obtained through the propagation of errors in the expression (3.8).

As we can see, the systemic velocity for PNe is lower than the stellar background in all galaxies in a similar ratio for all of them. This discrepancies are influenced by the shifted in wavelength which implies an uncertainty in the determination of the systemic velocity. Therefore, for all the galaxies there is an offset between the stars and the PNe. On the other hand, the asymmetry in the number of detected PNe in one side with respect to the other favours the presence of this offset, because the average value over all detections implies what those regions of the galaxy with more detections weights more than the other.

2.2. Velocity dispersion and radial profiles of PNe and stars

In first approximation, we consider that the velocity dispersion of the PNe is the same as the stellar background along the LoS of the PNe. In this way, each bin in Figure 4.5 has an associated value for the velocity dispersion. We have to take into account that some PNe do not have its stellar counterpart because this does not fall in a region with stars. In this case the value for the velocity dispersion is associated to the nearest star (for simplicity). However, in the outer regions of the galaxy, the profile for velocity dispersion reaches a constant value, so for these cases we could consider the velocity dispersion for the halo of the galaxies.
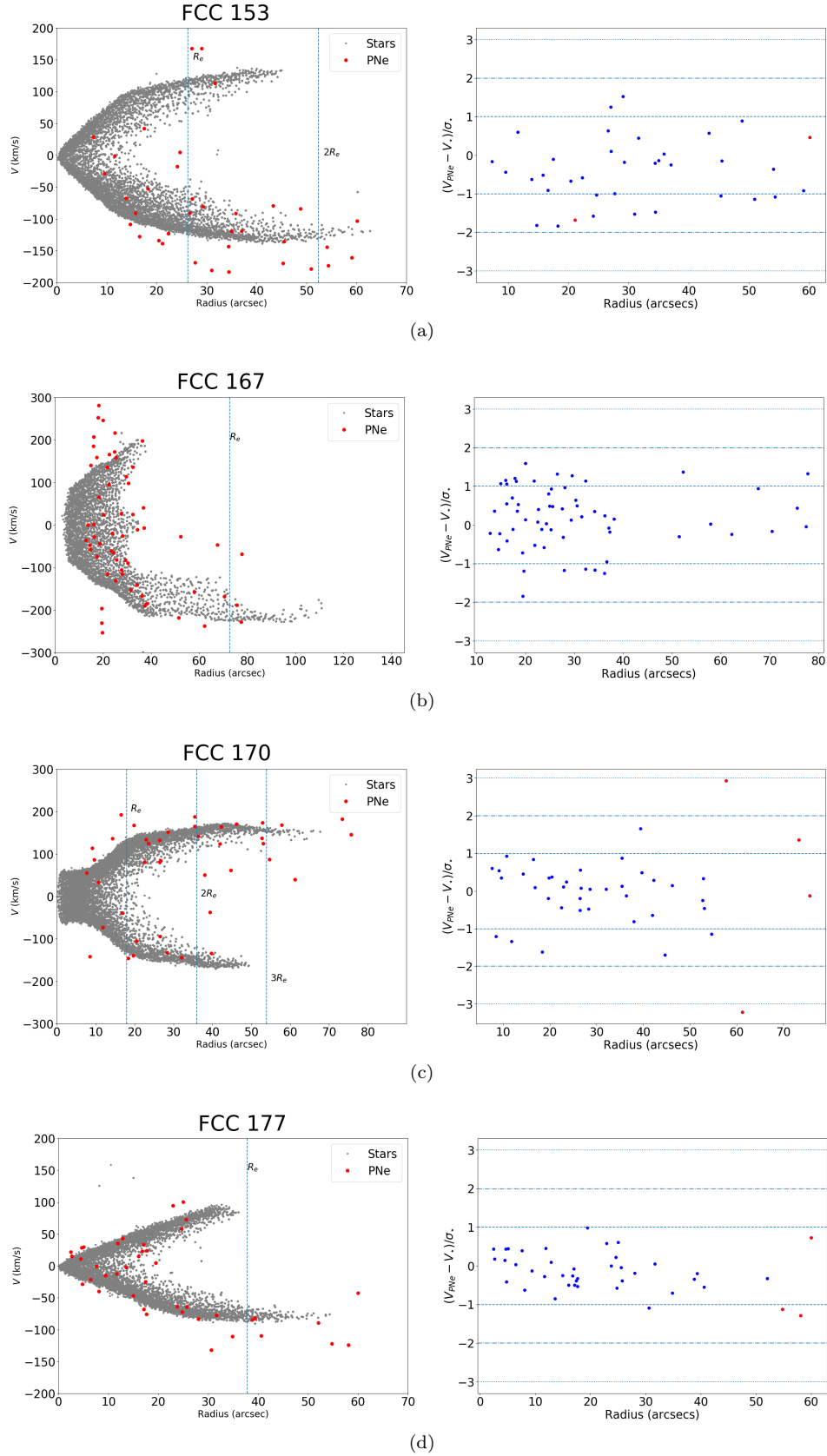
Figure 4.6: Radial profile of velocity and ratio between velocity and velocity dispersion of PNe for the four galaxies of study. The red dots in the velocity radial profiles indicate the kinematics of PNe while the grey dots represent the kinematics for stars. For the figures in the right column, the velocity of PNe are with respect to the velocity of the stellar background. The red dots represent the PNe which do not fall within the stellar background, and for so, the study of those objects is out of this work. The effective radii are given in Table 3.1.

Figure 4.6 shows the kinematics for PNe and the stellar background. In the right column we show the radial profiles of velocity for stars (grey dots) and PNe (red dots). In the left column, we plot the ratio between the velocity of each PN with respect to the stellar background and the velocity dispersion of them along the LoS.

With these results, we can compare figures 4.5 with figures 4.6. There is a clear agreement between the kinematics for stars and kinematics for PNe except for some outliers (red dots in dispersion maps) for which the velocity deviates with respect to the stars. However, the values of velocity for this outliers lies within reasonable numbers and do not deviates in more than 2σ except for FCC 170.

Galaxy	$(\mathbf{V_{PNe} - V_\star})/\sigma_\star \leq \mathbf{1}\sigma$	$(\mathbf{V_{PNe} - V_\star})/\sigma_\star \leq \mathbf{2}\sigma$	$\mathbf{N°}$ of outliers
FCC 153	24 (66.7%)	36 (100%)	2
FCC 167	43 (70.5%)	61 (100%)	0
FCC 170	32 (78.0%)	39 (95.1%)	4
FCC 177	38 (92.7%)	41 (100%)	3

Table 4.2: Number of PNe for different multiples of the dispersion along with the number of outliers for each galaxy. The first number represent the number of PNe within that sigma whereas the second ones represent the percentage of PNe with respect to the total detected.

In Table 4.2 we can observe the number of PNe which falls within 1σ and 2σ and the number of them with respect to the total of PNe (in percentage). Also, the number of outliers detected are tabulated too. In general, over the 95% of the PNe distribution falls within 2σ (Table 4.2), so there is a clear agreement between PNe and stellar background. Regarding FCC 153 and FCC 167 they have less than the 70% of the PNe within 1σ. However, for FCC 170 and FCC 177, the PNe percentage which falls within 1σ is greater than 75%. This result may be due by long tail in the PNe velocity dispersion which falls slowly from the center of the galaxy to the halo or an abnormal fall in velocity dispersion of the PNe for small radii.

For FCC 167 and FCC 170 the velocity profiles of the PNe adjusts to a Gaussian distribution for which around the 75% of the PNe are within 1σ. For FCC 153, we have fewer detections than we would expect to have so this may deviate the velocity distribution from a typical Gaussian distribution. Last, for FCC 177 the situation is abnormally "good": there are much more PNe within 1σ than we would expect. As we have already said, this may be dued by the shape of the velocity dispersion.

3. Analysis of luminosity function of the PNe

The LF of PNe is able to be estimated essentially measuring the total flux for each sample. These would give us a flux too low due to the level of noise. Therefore, we have recourse to the PSF of the instrument and we have calculated the flux applying Moffat 2D and Gaussian 1D models to our detections (see Section 2.1). Once this quantity is estimated, we can proceed with the LF without more than bin each PN with respect to the absolute magnitudes obtained.

3.1. Total luminosity function and comparison with the standard law

For the standard law, we draw on the equation (3.13) with the absolute magnitude values obtained through the spectra analysis. The amplitude of the standard law is calibrated for a good fit with the values observed.
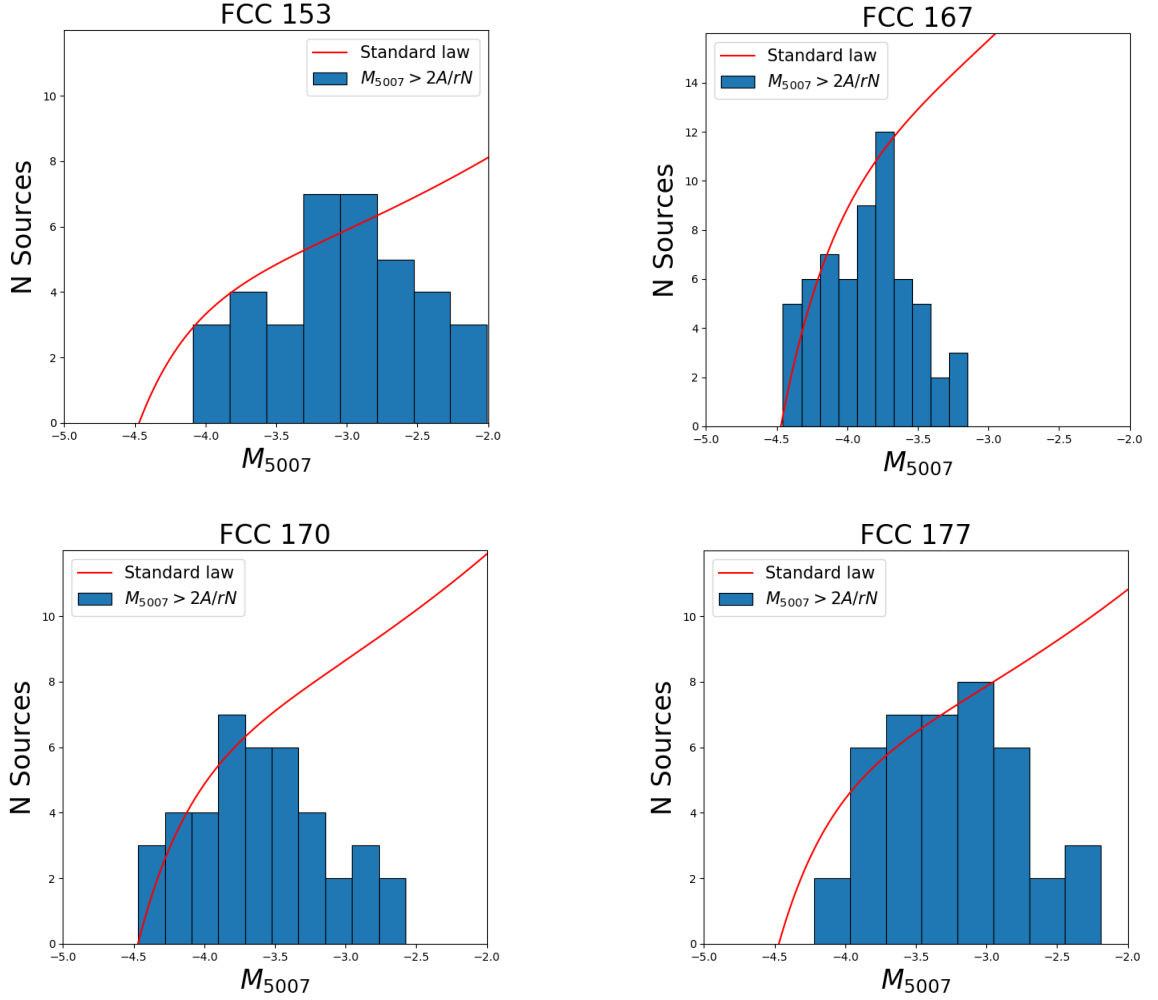
Figure 4.7: Absolute magnitude distribution of PNe along with the standard law (red line) given by (3.13). The absence of PNe in the bright end of the distributions is due to the incompleteness in absolute magnitude. The initial value for the standard law corresponds to $M^{\star}_{5007} = -4.47$.

Figure 4.7 shows the total luminosity function for the four galaxies. The red line is the standard law given by (3.13). As a result, we can observe a good fitting of the standard law and the detected PNe in function of the M_{5007} for the brightest PNe. However, for greater magnitudes than the maximum, the distribution deviates from the standard law due to the incompleteness of the PNe (Merrett et al., 2006; Sarzi et al., 2011).

Galaxy	Total number of PNe	$M^{\star}_{5007}$	$< M_{5007} >$	$M^{(max)}_{5007}$
FCC 153	36	-4.1 ± 0.1	-3.0 ± 0.1	-3.2 ± 0.1
FCC 167	61	-4.5 ± 0.1	-3.9 ± 0.1	-3.8 ± 0.1
FCC 170	41	-4.5 ± 0.1	-3.6 ± 0.1	-3.9 ± 0.1
FCC 177	41	-4.2 ± 0.1	-3.2 ± 0.1	-3.2 ± 0.1

Table 4.3: Absolute magnitudes and detected PNe for the four galaxies. The absolute magnitudes are estimated applying the Moffat 2D model with the estimated parameters for the PSF. Taking the flux of the [OIII] doublet we have calculated the apparent magnitude applying the equation (3.12), then with the distance modulus of Table 3.1 we obtain the absolute magnitude. $M^{\star}_{5007}$ is the absolute magnitude of the brightest PN for each galaxy, $< M_{5007} >$ is the mean absolute magnitude and $M^{(max)}_{5007}$ is the peak of the distribution. The errors in absolute magnitude are given by the uncertainty in flux for MUSE which is of 10% of the measured flux.

Table 4.3 tabulates both the number of detected PNe and the absolute magnitudes of them for the four galaxies. $< M_{5007} >$ is the mean value for the absolute magnitude of the [OIII] doublet[1] and $M_{5007}^{\star}$ is the absolute magnitude of the brightest detected PN.

For the four samples, we have a similar behaviour: modest amount of PNe for the brightest of these ones at $M_{5007} \leq -4.0$, a peak in the amount of PNe around $M_{5007} = -3.0, -4.0$ and then, a fall in the distribution from the maximum to the faint end of it.

We have to take into account that the standard law suffers a clear deviation for the observed distribution at the faintest regime. However, both the distribution and the standard law keep a good fit from the brightest PN to the peak of the absolute magnitude, where the number of PNe are the higher. Indeed, the detections obtained follow the standard law in a good degree of approximation, excluding the incompleteness at the faint end.

Particularly, for FCC 153 the number of detections in the halo is the lowest of the four samples of galaxies. These regions host the majority of the globular clusters of the galaxy, so in this case the contribution of blue-stragglers may be lesser abundant than for the other galaxies and, consequently this may affect to the value of the brightest PN in the LF. Moreover, there are not detected PNe close to the center of the galaxy due to the presence of dust. The absolute magnitude of the brightest PN in this galaxy is $M_{5007}^{\star} = -4.1$ which is the lowest value of the four galaxies and there is a certain incompleteness for the brightest magnitudes. Thus, if the brightest PNe were in the disk or near the center we would not be detecting these objects. So for this particular case, the shifted in magnitude to lower magnitudes in this galaxy may be due to the presence of dust in the disk.

The peaks in the distribution show that 167 and 170 have peaks around $M_{5007}^{(max)} = -3.8$ while 153 and 177 have the peaks in $M_{5007}^{(max)} = -3.2$. This implies that the LF falls from that peak in different magnitudes for the four galaxies. As the absolute magnitude is related with the mass of the progenitor stars, these results may indicate that the majority of PNe in 167 and 170 may proceed from a more massive progenitor population than 153 and 177, or maybe because this PNe are younger than the main nebular population of 153 and 177. We have to take into account that for 153 the presence of dust may be hidden more brighter PNe that are unobservable.

Respect to the absolute magnitude of the brightest PNe for 167 and 170, it is around $M_{5007}^{\star} = -4.5 \pm 0.1$, so in these cases, the both galaxies are in the limit of $M_{5007}^{\star} = -4.47$ established in Ciardullo et al. (1989). This nebular population may proceed from both intermediate mass progenitor stars and/or blue-stragglers due to the high luminosity of their brightest constituents.

Last, for 177 we are in an intermediate situation between the other two: the brightest PNe have an absolute magnitude of $M_{5007}^{\star} = -4.2 \pm 0.1$. In this case, the origin is not clear and this population may proceed from intermediate mass stars, blue-stragglers or even another solar-like progenitor population.

3.2.   Metallicity and absolute magnitude

The relation between the metallicity and the number of PNe may provide us a good key to understand the formation and the evolution of these objects as well as to understand the evolutionary traces of the galaxy in itself.

---

[1]We adopt this nomenclature for simplicity. However, the reader may observe here a discrepancy and think that we are just taking into account the 5007 line. This is not correct and we are calculating the absolute magnitude through the total amplitude of our Moffat model as we have described in the subsection 2.1.
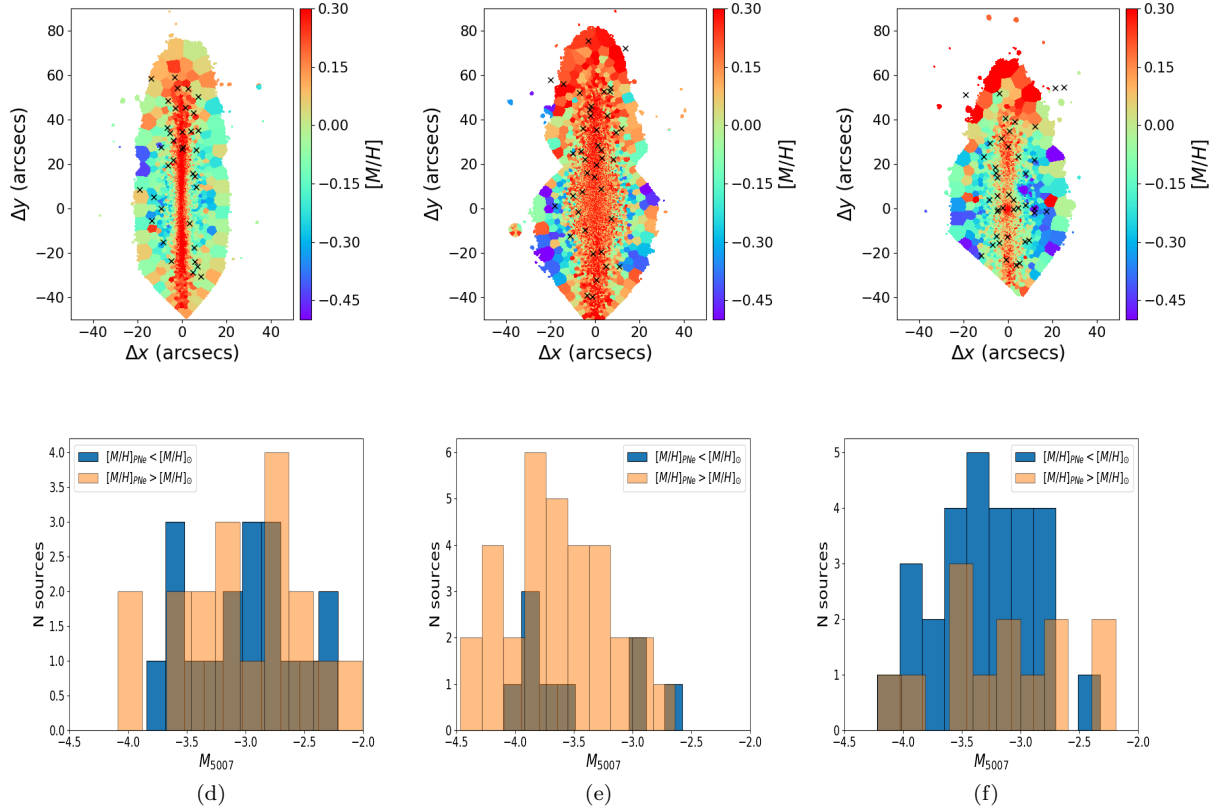
Figure 4.8: Comparison between metallicity and absolute magnitude. In the first row we show the metallicity maps of the stars obtained with *pPXF* and the PNe marked with black crosses. The second one, shows the absolute magnitude distribution for two populations of PNe: one metal-rich and one metal-poor (with respect to the solar metallicity). The metallicity is given in logarithmic scale. The column (a) represents the galaxy FCC 153. Column (b) is for FCC 170. Column (c) for galaxy FCC 177. In all cases, the metallicity is referred to the solar.

In Figure 4.8 we study the metallicity of FCC 153, FCC 170 and FCC 177. Unfortunately, we do not have enough data for FCC 167 to study the metallicity of it. The first row represents the metallicity maps of the stars obtained with *pPXF* and the PNe marked with black crosses. The second row shows the absolute magnitude distribution for two populations of PNe: one metal-rich and one metal-poor (with respect to the solar metallicity). The different columns represent these data for the three galaxies, namely: FCC 153 column (a); FCC 170 column (b); FCC 177 column (c). Particularly, for FCC 153 the low number of detections in the disk is due to the rescale of the spectra for the galaxy is not as correct as we would expect (see section 1) due to the presence of dust. For FCC 170 we have a metal-rich galaxy in which the majority of PNe fall within the disk, which is a metal-rich structure. Essentially, this is the reason because the distribution in magnitude is greater for $[M/H]_{PNe} > [M/H]_\star$ than $[M/H]_{PNe} < [M/H]_\star$. The incompleteness for the disk is produced for magnitudes such that $M_{5007} > -3.6$. For the halo, the number of detections is not enough to study the completeness.

In the three cases the brightest PNe are located in metal-rich regions and in the particular case of FCC 170 the brightest PN falls in the limit of $M_{5007} = -4.47$ whether for FCC 153 and FCC 177 the significance in the number of detections for the brightest PNe is too low to consider that the brightest limit falls within the metal-rich regions.

A high stellar metallicity can lead to a larger mass-loss rate efficiency in the RGB phase. This fact implies that the number of massive HB stars is lesser, and consequently the number of bright PNe is lesser too (Buzzoni et al., 2006; Pastorello et al., 2013). Essentially, this fact is the responsible of the lack of PNe in the bright end of the LF. This could be the situation which explains the lack of bright PNe in the disks of FCC 153 and FCC 177.

Galaxy	$< \mathbf{Z_{PNe}} >$	$< \mathbf{Z_\star} >$	$< \mathbf{Z_{PNe}} > / < \mathbf{Z_\star} >$
FCC 153	-0.013	0.251	-0.051
FCC 170	0.069	0.214	0.324
FCC 177	-0.093	0.158	-0.587

Table 4.4: Luminosity weighted metallicity for PNe and stellar background for FCC 153, FCC 170 and FCC 177. The values for the luminosity weighted metallicity are given by equation (3.14) for PNe and the stellar background.

In Table 4.4 we tabulate the values for the parameter $< Z >$, given by equation (3.14) for PNe and the stellar background. This quantity is obtained summing the flux for each bin and the metallicity estimated for each PNe. The three galaxies have positive values for $< Z_\star >$. This implies that the stars in the disk contributes more than the stars in the halo due to the high luminosity of the disk stars.

For 153, the lack of PNe in the disk implies that the halo, which is a metal-poor region, contributes more than the disk. This reason explain the negative value for $< Z_{PNe} >$. For 177 we are in the same situation. For FCC 170, the majority of PNe fall within the disk, in metal-rich regions. In this case, the sign for $< Z_{PNe} >$ is the same than $< Z_\star >$. For FCC 177 we are in an intermediate situation for which we have $< Z_\star >$ positive but the majority of PNe are located in metal-poor regions, and for so, $< Z_{PNe} >$ is negative. This is consequence that the majority of the PNe falls within the regions with lesser metallicity than Sun. For metal-rich PNe the number of samples are too low to analyse their completeness.

The lack of PNe in some regions of the studied galaxies affects to the completeness of our LF. In general terms, the main issue for this analysis is the low significance in the number of detections.

Conclusions

In this work, we have studied the LF of PNe for four early-type galaxies of the Fornax cluster. With the extraction of the continuum and the analisys of the [OIII] doublet we are able to observe the different PNe which populate the galaxies. These objects allow us to study the luminosity function, characteristic of these kind of objects, as well us the kinematics of the host galaxy.

The determination of PSF for the different pointings in which consist each galaxy permits us to go deep in flux for the different detections. With this method, we can get a good estimation of the value of the absolute magnitude for the PNe, and consequently, we can determine with a good accuracy, the absolute magnitude of the PNe.

The kinematics has been studied through the estimation of the shifted [OIII] lines for all the PNe, while the kinematics for the stellar background has been calculated through $pPXF$ algorithm. The comparison between these two components are in a good agreement from the inner disk of the galaxies and beyond there. The exceptions are the detected outliers in FCC 153, FCC 170 and FCC 177 for which we cannot contribute with any information about their kinematics. These kind of detections are inconsistent with the consideration of velocity dispersion. The position of the PNe affects to the kinematics estimation too, due to the inhomogeneities in the distribution of them. In fact, for FCC 170 and FCC 177 there is a good correlation between them with more than a 75% of the PNe within 1σ, while for FCC 153 and FCC 167 the majority of PNe are between 65% and 70% due, precisely to this inhomogeneities. In general terms, the kinematics of PNe follows the movement of the stars of the galaxies.

As we have observed, the shape of the PNe distribution in magnitude are related with the observational law given by Ciardullo et al. (1989) through the absolute magnitude of the brightest [OIII] doublet. The value for this parameter is well established thank to different theoretical model of PNe evolution as (Merrett et al., 2006) and corresponds to $M^{\star}_{5007} = -4.47$. This value represents a fundamental parameter to use the LF as second order distance calibrator due to the well established value of the brightest PNe for ETGs. Essentially, the presence of the brightest PNe is due to a progenitor stars of intermediate mass and/or the presence of blue-stragglers. These last ones are common objects in the ETGs. The both ones may be the progenitor population of the brightest PNe detected in the four galaxies.

The metallicity of the galaxies represents a tool to corroborate the nature of the PNe: their origin and evolution. Moreover, metallicity provides us the clues to relate the light of the PNe with the metallicity due to the progenitor stars. Nevertheless, the significance in the number of detections is not enough. Consequently, we cannot split the halo PNe from the disk PNe in order to study both components separately. The only consequence we have deduced from this analysis is that the brightest PNe are placed in metal-rich regions, however the low number of detected PNe does not permit us to make any hypothesis about this fact.

While the LF gives us information about the different possible populations of progenitor stars which formed the PNe, the kinematics permits to study the own movement of the whole galaxy. Essentially, the PNe represent a good key to unveil the properties of formation and evolution of the galaxies thanks to the well established physical properties of their formation and the singular nature of their light.

It should be noted that this work is a preamble to the study of the whole galaxies of the Fornax cluster through the data provided by Fornax3D. Through the whole sample of galaxies, we will be able to improve our study and get a better understanding about the origin of the PNe as well as their relation with their environment.

Bibliography

Binney, J. and Merrifield, M. (1998). *Galactic astronomy*. Princeton University Press.

Blakeslee, J. P., Jordán, A., Mei, S., Côté, P., Ferrarese, L., Infante, L., Peng, E. W., Tonry, J. L., and West, M. J. (2009). The acs fornax cluster survey. v. measurement and recalibration of surface brightness fluctuations and a precise value of the fornax-virgo relative distance. *The Astrophysical Journal*, 694(1):556.

Bowen, I. S. (1927). The origin of the nebulium spectrum. *Nature*, 120(3022):473.

Buzzoni, A., Arnaboldi, M., and Corradi, R. L. (2006). Planetary nebulae as tracers of galaxy stellar populations. *Monthly Notices of the Royal Astronomical Society*, 368(2):877–894.

Cappellari, M. (2009). Voronoi binning: Optimal adaptive tessellations of multi-dimensional data. *arXiv preprint arXiv:0912.1303*.

Cappellari, M. and Emsellem, E. (2004). Parametric recovery of line-of-sight velocity distributions from absorption-line spectra of galaxies via penalized likelihood. *Publications of the Astronomical Society of the Pacific*, 116(816):138.

Ciardullo, R., Durrell, P. R., Laychak, M. B., Herrmann, K. A., Moody, K., Jacoby, G. H., and Feldmeier, J. J. (2004). The planetary nebula system of m33. *The Astrophysical Journal*, 614(1):167.

Ciardullo, R., Feldmeier, J. J., Jacoby, G. H., de Naray, R. K., Laychak, M. B., and Durrell, P. R. (2002). Planetary nebulae as standard candles. xii. connecting the population i and population ii distance scales. *The Astrophysical Journal*, 577(1):31.

Ciardullo, R., Jacoby, G. H., Ford, H. C., and Neill, J. D. (1989). Planetary nebulae as standard candles. ii-the calibration in m31 and its companions. *The Astrophysical Journal*, 339:53–69.

Ciardullo, R., Sigurdsson, S., Feldmeier, J. J., and Jacoby, G. H. (2005). Close binaries as the progenitors of the brightest planetary nebulae. *The Astrophysical Journal*, 629(1):499.

Coccato, L., Gerhard, O., Arnaboldi, M., Das, P., Douglas, N. G., Kuijken, K., Merrifield, M., Napolitano, N., Noordermeer, E., Romanowsky, A., et al. (2009). Kinematic properties of early-type galaxy haloes using planetary nebulae. *Monthly Notices of the Royal Astronomical Society*, 394(3):1249–1283.

Ferguson, H. C. (1989). Population studies in groups and clusters of galaxies. ii-a catalog of galaxies in the central 3.5 deg of the fornax cluster. *The Astronomical Journal*, 98:367–418.

Jacoby, G. H. (1989). Planetary nebulae as standard candles. i-evolutionary models. *The Astrophysical Journal*, 339:39–52.

Kuntschner, H., Emsellem, E., Bacon, R., Cappellari, M., Davies, R. L., de Zeeuw, P. T., Falcón-Barroso, J., Krajnović, D., McDermid, R. M., Peletier, R. F., et al. (2010). The sauron project–xvii. stellar population analysis of the absorption line strength maps of 48 early-type galaxies. *Monthly Notices of the Royal Astronomical Society*, 408(1):97–132.

Kwok, S. (2007). *The origin and evolution of planetary nebulae*. Cambridge University Press.

Mapelli, M., Sigurdsson, S., Ferraro, F. R., Colpi, M., Possenti, A., and Lanzoni, B. (2006). The radial distribution of blue straggler stars and the nature of their progenitors. *Monthly Notices of the Royal Astronomical Society*, 373(1):361–368.

Marigo, P., Girardi, L., Weiss, A., Groenewegen, M., and Chiosi, C. (2004). Evolution of planetary nebulae-ii. population effects on the bright cut-off of the pnlf. *Astronomy & Astrophysics*, 423(3):995–1015.

Merrett, H. R., Merrifield, M., Douglas, N., Kuijken, K., Romanowsky, A. J., Napolitano, N., Arnaboldi, M., Capaccioli, M., Freeman, K., Gerhard, O., et al. (2006). A deep kinematic survey of planetary nebulae in the andromeda galaxy using the planetary nebula spectrograph. *Monthly Notices of the Royal Astronomical Society*, 369(1):120–142.

Pastorello, N., Sarzi, M., Cappellari, M., Emsellem, E., Mamon, G. A., Bacon, R., Davies, R. L., and de Zeeuw, P. T. (2013). The planetary nebulae population in the nuclear regions of m31: the sauron view. *Monthly Notices of the Royal Astronomical Society*, 430(2):1219–1229.

Pulsoni, C., Gerhard, O., Arnaboldi, M., Coccato, L., Longobardi, A., Napolitano, N., Narayan, C., Gupta, V., Burkert, A., Capaccioli, M., et al. (2017). The extended planetary nebula spectrograph (epn. s) early-type galaxy survey. the kinematic diversity of stellar halos and the relation between halo transition scale and stellar mass. *arXiv preprint arXiv:1712.05833*.

Rodríguez-González, A., Hernández-Martínez, L., Esquivel, A., Raga, A., Stasińska, G., Peña, M., and Mayya, Y. (2015). A two-mode planetary nebula luminosity function. *Astronomy & Astrophysics*, 575:A1.

Rosenfield, P., Johnson, L. C., Girardi, L., Dalcanton, J. J., Bressan, A., Lang, D., Williams, B. F., Guhathakurta, P., Howley, K. M., Lauer, T. R., et al. (2012). The panchromatic hubble andromeda treasury. i. bright uv stars in the bulge of m31. *The Astrophysical Journal*, 755(2):131.

Sarzi, M., Mamon, G. A., Cappellari, M., Emsellem, E., Bacon, R., Davies, R. L., and Tim de Zeeuw, P. (2011). The planetary nebulae population in the central regions of m32: the sauron view. *Monthly Notices of the Royal Astronomical Society*, 415(3):2832–2843.

Schönberner, D., Jacob, R., Steffen, M., and Sandin, C. (2007). The evolution of planetary nebulae-iv. on the physics of the luminosity function. *Astronomy & Astrophysics*, 473(2):467–484.

Spiniello, C., Napolitano, N., Arnaboldi, M., Tortora, C., Coccato, L., Capaccioli, M., Gerhard, O., Iodice, E., Spavone, M., Cantiello, M., et al. (2018). The fornax cluster vlt spectroscopic survey ii–planetary nebulae kinematics within 200 kpc of the cluster core. *Monthly Notices of the Royal Astronomical Society*, 477(2):1880–1892.

Vazdekis, A., Sánchez-Blázquez, P., Falcón-Barroso, J., Cenarro, A., Beasley, M., Cardiel, N., Gorgas, J., and Peletier, R. (2010). Evolutionary stellar population synthesis with miles–i. the base models and a new line index system. *Monthly Notices of the Royal Astronomical Society*, 404(4):1639–1671.

Appendices

Appendix A

Detected PNe

In this chapter we show all the detected PNe for the four galaxies. The counts per pixel are obtained with no more than sum the flux for the spectrum of each pixel. These counts are normalized to unity to smooth the spatial distribution. In this way, we minimize the differences between the highest negative value and the highest positive value.
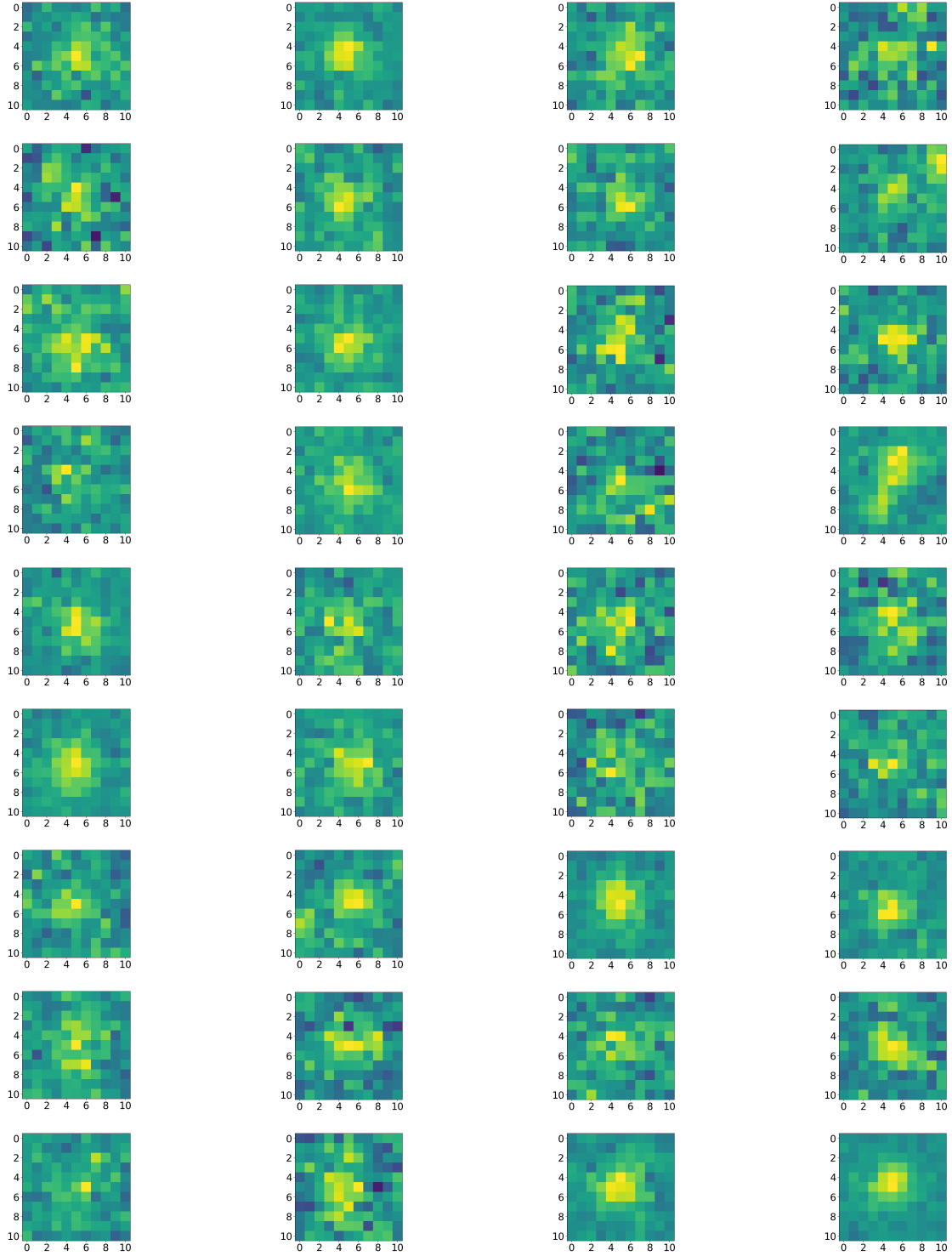
1. FCC 153

Figure A.1: detected PNe for FCC 153. The counts per pixel are normalized to the maximum value of the whole window.
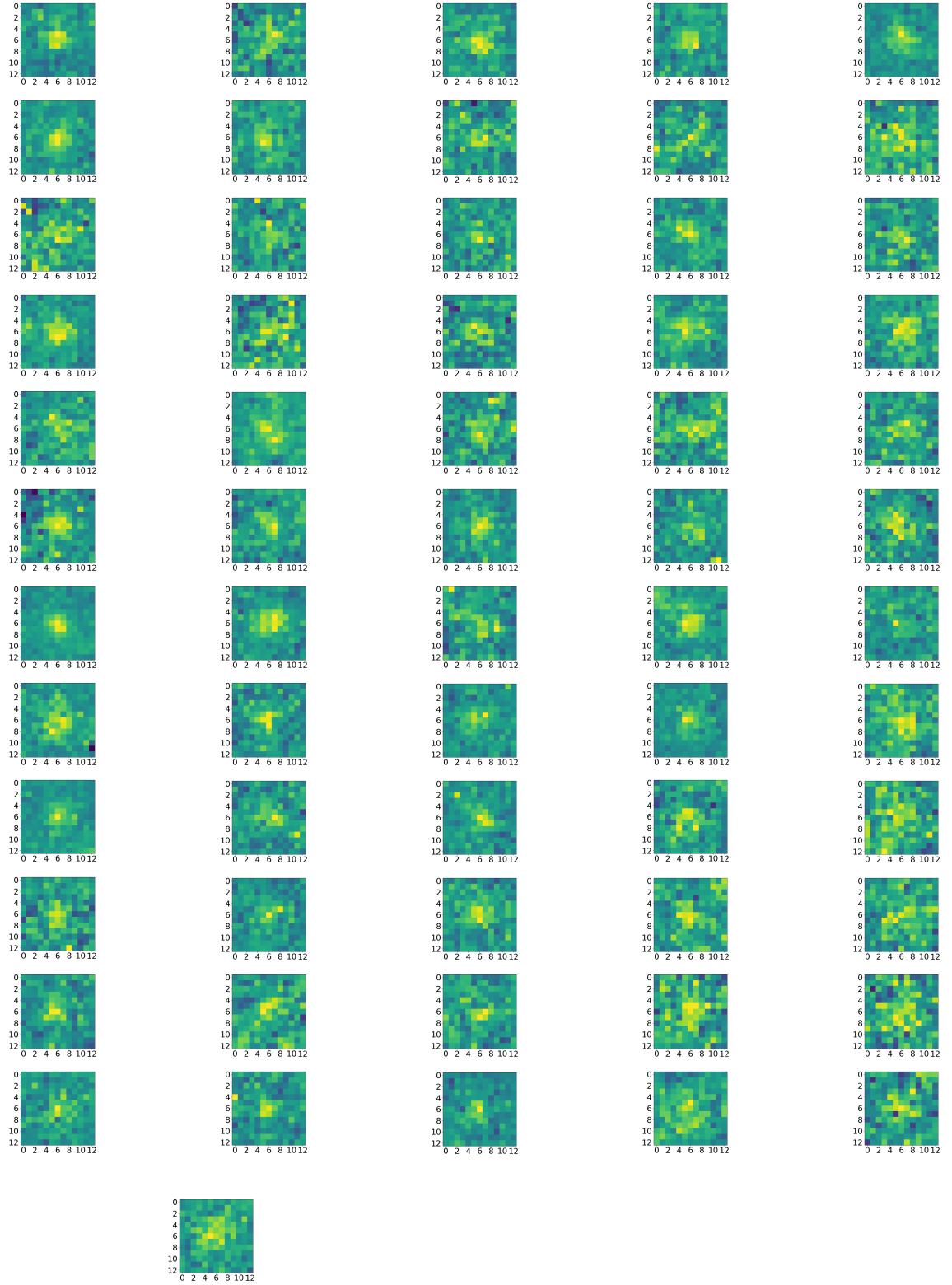
2. FCC 167

Figure A.2: detected PNe for FCC 167. The counts per pixel are normalized to the maximum value of the whole window.
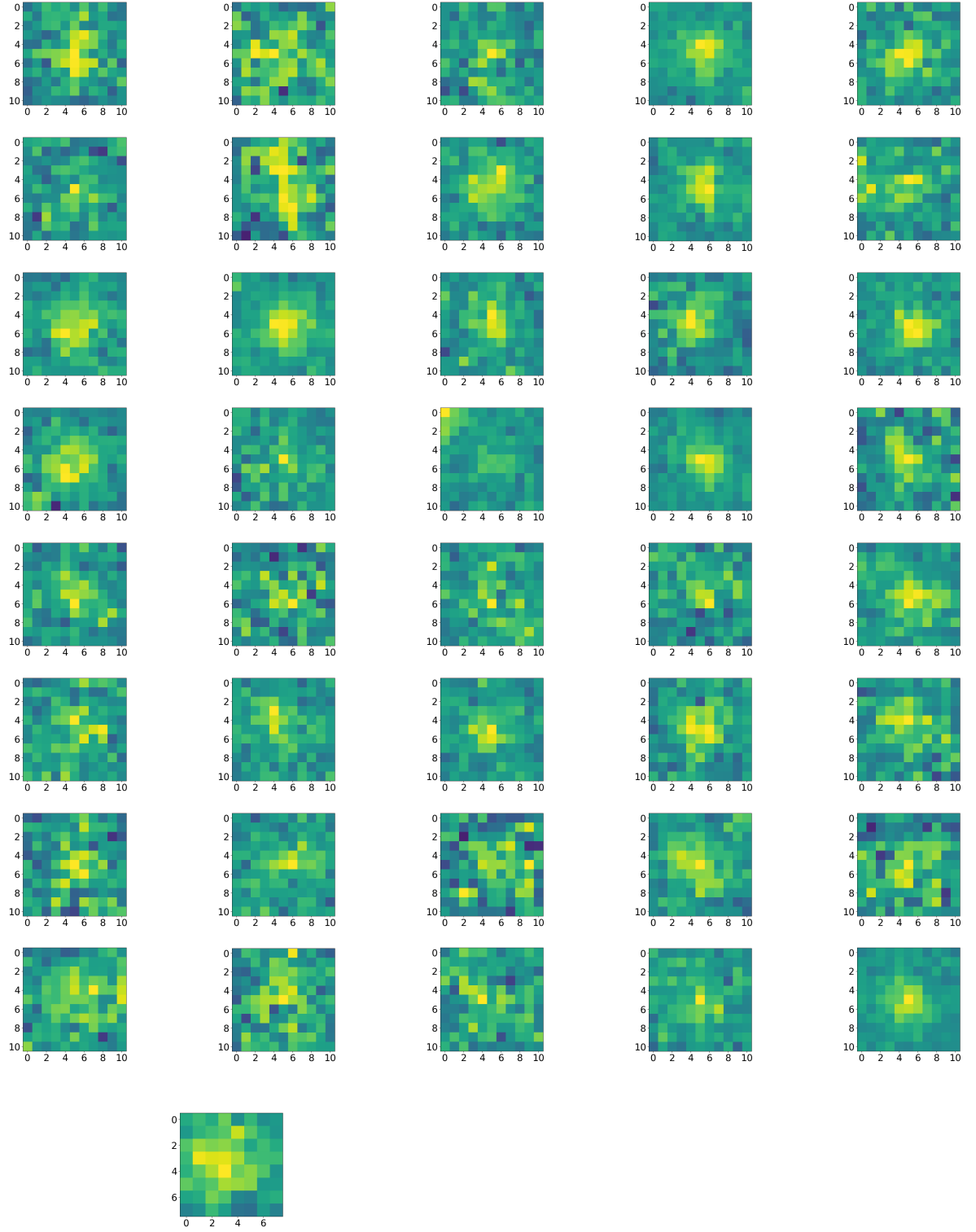
3. FCC 170

Figure A.3: detected PNe for FCC 170. The counts per pixel are normalized to the maximum value of the whole window.
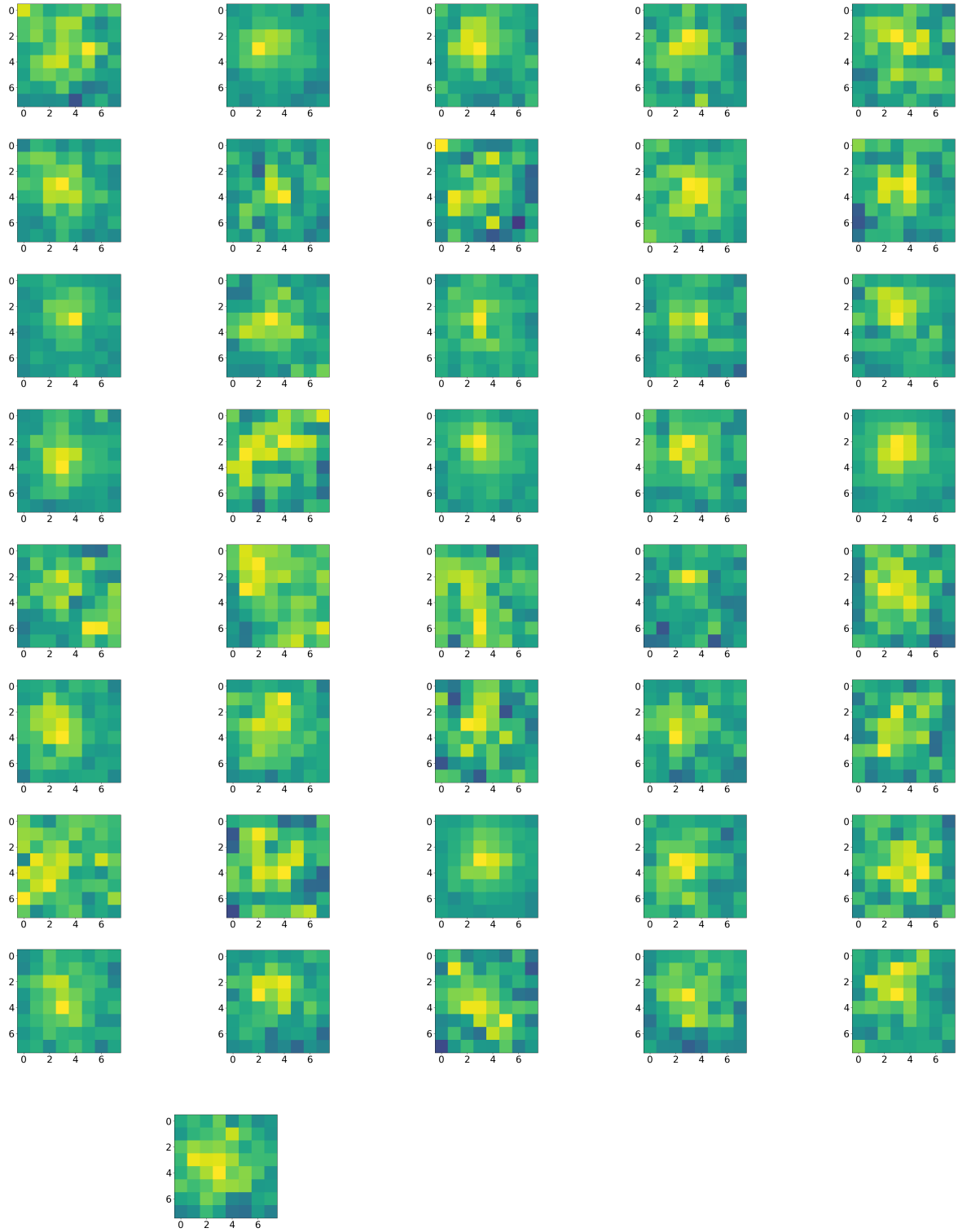
4. FCC 177

Figure A.4: detected PNe for FCC 177. The counts per pixel are normalized to the maximum value of the whole window.